

MSc Thesis, Department of Soil, Geography and Landscape
Wageningen UR

Towards accurate dating of Holocene basalt sequences by feldspar OSL: A case study at Isla de Pico (Azores)

Author:

Elaine Sellwood

Student ID: 9208168030

Supervisors:

Dr. Benny Guralnik

Dr. Tony Reimann

Dr. Lennart de Groot



Abstract

The dynamic nature of the Earth's Magnetic Field can lead to unexplained magnetic behaviours such as polar reversals and field intensity fluctuations. With reliance on the magnetic field stretching from man-made GPS systems to migratory animals (Lohmann, et al., 2004) it is important to determine what happens when the field changes, and increase the resolution of the current palaeo-intensity record. Conventionally, palaeo-intensity measurements are constrained with radiocarbon ages, endorsed for its short 5730 ± 40 a half-life (Grootes, 2015), but such material can become contaminated by older/younger material or inappropriately matched to other stratigraphic units. Conventional Thellier-style intensity protocols include various heating stages during measurement, which can thermally alter the minerals natural magnetic signature (Thellier & Thellier, 1959).

Presented here are the results from feldspar luminescence dating protocols from Tsukamoto et al, (2011), used to temporally constrain palaeo-magnetic intensity data, obtained using the Pseudo-Thellier relative intensity approach (De Groot, et al., 2013) using basalt ≤ 3.86 ka in age from the Island of Pico. Three samples were dated with IRSL₅₀ at 2.64 ± 0.41 ka (PI-07), 1.55 ± 0.49 ka (PI-12) and 3.05 ± 1.19 ka (PI-19), with PI-12 and -19 overlapping their ¹⁴C ages of 1.65 and 3.86 ka respectively (Nunes, 1999). The PI-07 IRSL₅₀ age overestimates the 0.3 ka ¹⁴C age, possibly due to a compositional mix with older xenocrysts. The Ca-rich plagioclase composition made signal characterisation difficult, with dim natural and noisy regenerated emissions. Eight palaeo-intensity values between 23.1- 64.4 μ T, and 15 directional values were obtained using the Pseudo-Thellier approach. Six of the points plotted with ¹⁴C ages and 1 point with the PI-07 IRSL₅₀ age, to within confidence intervals of same-sample data from different Thellier-style methods and with three geo-magnetic reference models. The results validate the use of IRSL₅₀ dating of basaltic feldspars, alongside Pseudo-Thellier measurements to produce absolute chronologies of the characteristics of the Earths' Magnetic Field over the late Holocene, and both methods should be refined further, increasing the resolution of the current palaeo-magnetic record.

Table of Contents

Abstract	2
List of Figures	4
List of Tables	7
Abbreviations	7
Units/Notation	8
1. Introduction	9
1.1 Research aims and objectives	9
1.2 Geological Setting	11
1.3 Sample Locations	12
2. Petrology and Mineralogy	16
2.1 Introduction	16
2.2 Theoretical background	17
Michel-Levy	17
SEM and EDS	18
VSM	18
2.3 Applied Methodology	20
2.4 Results	22
Microscopy	22
SEM and EDS	22
Dose rate determination	25
VSM	26
2.5 Discussion	27
3. Luminescence	29
3.1 Introduction	29
3.2 Theoretical background	30
3.3 Applied methodology	32
3.4 Results	34
3.5 Discussion	39
4. Palaeo-Magnetic Intensity	42
4.1 Introduction	42
4.2 Theoretical Background	43
4.3 Applied Methodology	46
4.4 Results	47
Directional Data	51

4.5 Discussion	55
5. Synthesis and discussion	57
5.1 Synthesis.....	57
Discussion	62
Mineralogy, Petrology and Dose rate.....	62
Mineralogy, petrology and OSL.....	62
Pseudo-Thellier and OSL.....	64
Mineralogy, petrology and Pseudo-Thellier.....	65
5.2 Conclusion.....	66
Acknowledgements	67
Bibliography	68

List of Figures

Figure 1.2.1. Classification of volcanic units from the Island of Pico (França, et al., 2006).	11
Figure 1.3.1. A) Location of the South Atlantic Anomaly, and proximity to the Azores (star) (Lemoine & Capdeville, 2006). B) Sketch of Azores located on the Azores triple junction, and proximity to Terceira (Miranda, et al., 1998). C) Map of main volcanic units modified from Quartau, et al., (2015) with all Pico sample locations. Yellow diamonds are the ones selected for luminescence dating. D) Sampling method used by BSc students at Utrecht University.	13
Figure 2.1.1 Bowens reaction series, with decreasing temperatures and increasing SiO ₂ in the directions of the arrows. (Bowen, 1922)	16
Figure 2.1.2 Ternary plot of Fe-Ti-Oxides (Franke, et al., 2007).	17
Figure 2.2.1 Graph used with Michel-Levy measurements to determine the abundance of Na and Ca. Dotted line is to be used with volcanic samples, and the solid line is for use with plutonic samples. (Nesse, 2000).....	18
Figure 2.2.3 A) example of a hysteresis plot, with the demagnetisation and re-magnetisation curves plotted and HC (field coercivity), Mrs (remnant magnetic saturation) and Ms (magnetic saturation) values obtained. And B) DCD curve, with the Hcr (remnant coercivity) value obtained as it crosses the X axis.....	19
Figure 2.2.2 . Example of a Day plot from (Dunlop, 2002) with domain boundaries defined and theoretical mixing curves for magnetite as they crystallise.....	19
Figure 2.3.1. Geological map with literature and own sample locations used for literature dose rate determination. Left: Table with paired own and literature samples.	21
Figure 2.4.1 Examples of images from the Leica Polarising microscope. Left: Plain polarised light, right: crossed polarised light. A) PI-08 lacking significant phenocryst phases, with abundant magnetic	

minerals. B) PI-04 with only olivine and pyroxene phenocrysts and a coarse feldspar-rich groundmass. C) PI-19 with large plagioclase phenocrysts and a coarse groundmass (>0.5mm). PI: plagioclase, Ol: olivine, Opt: opaque minerals, Ilm: Ilmenite, Cpx: clinopyroxene. 23

Figure 2.4.2 A) Ternary plot of Michel-Levy results from measured phenocrysts in samples PI-07, -12 and -19. Points are plotted on the Ab-An axis as Or% is not known. B) Ternary plot of all EDS results, with all measured plagioclases >50An%..... 24

Figure 2.4.3 Matching of Leica (left: plain polarised light, right: crossed polars) and SEM/EDS measurements, an example of a plagioclase crystal patch from sample PI-12, and the point measurements which were taken..... 25

Figure 2.4.4 Day plot displaying domain properties from the VSM of measured magnetic minerals. Domain boundaries are taken from (Day, et al., 1977). All results fall on a mixing curve of SD and MD grains, indicating a mix of small- medium grain sizes..... 26

Figure 3.1.1 Examples of A) Thermoluminescence peak, and B) IRSL decay curve taken at room temperature from a pegmatite-sourced K-feldspar (Ademola, 2014)..... 29

Figure 3.2.1. Schematic diagram of the movement of electrons between the valence and conductance bands, with the presence of ‘traps’ (1), and the release of the photon as they move between energy states. (Preusser, et al., 2008) 30

Figure 3.2.2. Example of a dose response curve and interpolated De. (Tsukamoto, et al., 2011) 31

Figure 3.3.1 Example of a natural pIRIR signal from sample PI-07. No decay components are seen in any natural or regenerative signals, which were all dim and noisy..... 33

Figure 3.4.1 A: TL curve produced from PI-07, (50-90µm). No SAR stages were performed during this sequence. B: TL peak from PI-12, (63-90µm), small peak and noisy signal. C: Natural decay curve from PI-19 (63-90µm) after the first round of density separation. 35

Figure 3.4.2 Examples of natural and regenerated decay curves, dose response curves and Tx/Tn plots to show sensitivity. An example Lx/Tx graph from the fading test is also included for each sample on the far right. Top row shows PI-07 examples of a high extrapolated De value in response to high laboratory doses, which is also seen in the drop in sensitivity with the first SAR cycle, and response to lab doses. 37

Figure 3.4.3. Left: Natural Pulsed BLSL decay curve from sample PI-12, showing a small and noisy emission obtained over the whole pulsed stimulation period. Right: Distribution of photon arrival times between gating times for the natural pulsed BLSL step. No clear quartz or feldspar decay component is seen; with the sharp decrease in photon counts around bin 45-50 possibly a product of the switching off of the stimulation, or may indicate the presence of unsensitised quartz (Guralnik, et al., 2015)..... 38

Figure 4.1.1 Magnetic Vectors. X: North component, Y: east component, Z: vertical intensity, D: declination, F: total intensity, H: horizontal intensity and, I: Intensity. (NGDC, 2016) 42

Figure 4.2.1 Calibration curve and equation used for relative to absolute PMI calibration. (de Groot, et al., 2016)..... 44

Figure 4.2.2 pTh results normalised with the Global Geomagnetic reference field over B1/2 ARM values. Between 23 and 63mT, there is a linear and stable relationship between the pTh results and

B1/2 ARM values. (De Groot, et al., 2013), and these limits are used to separate accepted and rejected pTh PMI values.	45
Figure 4.2.3 A) Example of Zijderveld diagram, with linear vectors and no directional changes or secondary NRMs observed. The inclination is not determinable from this graph B) Example of an equal-area projection plot where there is a very small wander of the vectors. The declination can be read from the outer circle, and the inclination from the vertical axis. Both plots are from paleomagnetism.org.	46
Figure 4.3.1 Flow chart of stages for pTh measurement, with values of step-wise field application. ..	47
Figure 4.4.1 Example arai-style plots from PI-14, -07 and -19 and corresponding Zijderveld diagrams, equal area projection (EAP) plots and summary directional circles. PI-14 shows a strong change in magnetisation after the first 2 steps, and some directional wander in the EAP. PI-19 shows differences in NRM demagnetisation over ARM gained, with one sample showing anomalous directional behaviour.	48
Figure 4.4.2 Range of PMI (μ T) values produced from all samples, and display of whether these values passed or failed the first statistical criteria, and comparison with the expected field.	49
Figure 4.4.3 Comparison of the IZZI- and Microwave-Thellier results with the Pseudo-Thellier results obtained here. Vertical and horizontal error bars represent PMI sigma values.	50
Figure 4.4.5 E.g. Zijderveld diagram from PI14- X1 with a change in magnetisation after the first demagnetisation step.	51
Figure 4.4.4 Final plot of achieved pTh PMI values paired with OSL ages (red circles), with results from neighbouring islands of Terceira (de Groot, et al., 2016), and Sao Miguel (Di Chiara, et al., 2014) and from the BSc thesis of van Grinsven, (2016) and Gülcher (2016). Reference geomagnetic field models are also plotted with the radiocarbon ages. The shading indicates 1σ confidence bands.	52
Figure 4.4.6 A) Declination from this study and the BSc thesis from Wassing, (2016), with 3 reference models. B) Inclination data with reference models. Vertical errors show α_{95} errors, and horizontal errors are 1σ probability intervals from the Radiocarbon calibration.	54
Figure 5.1.1. Palaeo-magnetic intensity changes over the past 3ka, from the Pseudo-Thellier measurements and calibrated 14 C ages. Red and blue lines indicate reference geomagnetic field models SHA.DIF.14K, PFM9K.1b and IGRF12. Shading indicates 1 standard deviation confidence limits. The one paired OSL and pTh result is plotted (Pink triangle, PI-07 OSL age). The PI-07 and PI-12 OSL ages were also paired with results from the IZZI-Thellier tests (blue square and purple diamond).....	60
Figure 5.1.2 Top: OSL ages paired with pTh and the BSc results from Wassing,(2016), as well as all inclinations plotted over the calibrated radiocarbon ages. Bottom: Same as top but for Declination...	61

List of Tables

Table 1.3.1. Summary of all sample locations, with coordinates, radiocarbon and calibrated ages, with corresponding 1σ probability intervals. Source references for the radiocarbon ages are given, along with what the samples were used for in this study. Ages in brackets are the minimum ages used for data presentation.....	15
Table 2.4.1. Summary of Literature and measured dose rates for the 4-11 μm fraction.....	26
Table 3.3.1 Summary of sequences run in this study, from Tsukamoto, et al., (2011).....	32
Table 3.4.1 Weighted mean and median D_e 's (Gy) and respective ages.....	36
Table 4.4.1 Summary results from the Pseudo-Thellier PMI tests for the Pico samples. Individual sample PMI values are show, along with the final averaged PMI value per age group, standard deviation and beta (sigma/average) values.....	49
Table 4.4.2 Summary table of magnetic declinations and inclinations achieved from the pTh NRM demagnetisation data. Accepted data is in black, rejected value ($k < 50$ or >1000) are in blue.....	53
Table 5.1.1. Summary of all achieved IRSL_{50} ages and Pseudo-Thellier PMI and directional results with corresponding calibrated radiocarbon ages. Average anorthite % from EDS measurements and the domain states from the VSM results are stated. PMI and/or directional values for the other four basalts are also provided from literature.	59

Abbreviations

ARM	Anhyseretic Remnant Magnetism/ Magnetisation
BLSL	Blue Light Stimulated Luminescence
Cpx	Clinopyroxene
D	Declination
D_e	Dose Rate
D_R	Equivalent Dose
EDS	Energy Dispersed Spectroscopy
EMF	Earths' Magnetic Field
Hc	Field Coercivity
Hcr	Remanent coercivity
I	Inclination
Ilm	Ilmenite
IRSL_{50}	Infra-Red Stimulated Luminescence at 50°C
Mrs	Remanent Magnetic Saturation
Ms	Magnetic Saturation

NRM	Natural Remnant Magnetism/ Magnetisation
OI	Olivine
Opq	Opaque minerals
OSL	Optically Stimulated Luminescence
pIRIR	Post Infra-Red Stimulated Luminescence
Pl	Plagioclase
PMI	Palaeo-Magnetic Intensity
pTh	Pseudo-Thellier
SAR	Single Aliquot Regeneration protocol
SEM	Scanning Electron Microscope
TL	Thermoluminescence
VSM	Vibrating Sample Magnetometer

Units/Notation

B	Magnetic Flux Intensity
H	Magnetic field intensity or strength
Gy	Gray, absorption of 1 joule of radiation per kg of material.
Ka	Kilo annum
mT	Milli-Tesla, for relative B field values
μ T	Micro-Tesla, for absolute B field values.
Oe	Oersted, unit for H
emu	'Electromagnetic unit', sometimes used as a magnetic moment
Decimal Degrees	For palaeo-directional data

1. Introduction

1.1 Research aims and objectives

The dynamic nature of the Earth's Magnetic Field can lead to the development of strange magnetic behaviours such as global-scale polar reversals and localised field intensity fluctuations. With reliance on the magnetic field stretching from man-made GPS systems to migratory animals (Lohmann, et al., 2004) it is important to determine what happens when the field intensity changes, and increase the resolution of the current palaeo-intensity record. Utilising dated geological materials such as igneous and volcanic deposits, occurrences of such unexplainable global phenomena have been seen throughout the 3.2 Ga palaeo-intensity record (Tarduno, 2007). Appropriate magnetic minerals must be available to address the past intensities, but over the Pacific and Atlantic Oceans a lack of accessible materials has inhibited the full exploration of such localised magnetic events. The presence of the South Atlantic Magnetic Anomaly (SAMA) wandering between South America and Africa calls for more data and information on the cause and effects of a low magnetic field intensity on life and planetary systems. Recent volcanism has occurred within the past century in the Atlantic, and exploration of magnetic minerals from these basaltic accumulations poses a promising opportunity for producing a high-resolution documentation of a localised magnetic anomaly.

Holocene-age palaeo-magnetic intensity (PMI) measurements conventionally use methods developed by Thellier & Thellier, (1959) and are temporally constrained with radiocarbon (^{14}C) dates obtained from carbon based material which has been directly buried or stratigraphically matched to the measured unit. Using ^{14}C for dating has been favoured as it has a short half-life of $5730 \pm 40\text{a}$ (Grootes, 2015), suitable for dating of Late Pleistocene and Holocene age deposits. However, several difficulties may arise with obtaining reliable ages with possibilities of mismatching of the dated material to other stratigraphic units, or recycled carbonate material being transported in from older deposits, leading to age overestimates. Uncertainties in the results are also introduced from calibrating the ^{14}C ages, as the atmospheric $^{14}\text{C}/^{12}\text{C}$ ratios have not been constant over time and these fluctuations must be accounted for to produce absolute ages (Reimer, et al., 2013).

Conventional PMI measurement procedures such as the IZZI-Thellier and Microwave-Thellier methods (Thellier & Thellier, 1959) have contributed to the building of the current magnetic records and of models explaining the fields past and present behaviour. It has however been known that the pre-heating stages and thermal demagnetisation stages during intensity measurement can cause thermal alteration of the electron configurations in the magnetic minerals and lead to a secondary magnetic signature which must be corrected for.

With these problems in mind, there has been a call for more robust and accurate protocols for both fields which circumvent these issues. Here I assess the potential of pairing the novel pseudo-Thellier PMI method with feldspar Luminescence dating techniques using basalt, to better constrain local

geomagnetic intensity changes around the Island of Pico (Azores) over the past 3 ka of the Late Holocene. The main aims of this research are to:

- Characterise the luminescence signals from young Holocene age volcanic feldspars from basalt from Pico (Azores) using thermoluminescence (TL), optically stimulated luminescence (OSL) and infra-red stimulated luminescence (IRSL) protocols from Tsukamoto, et al, (2011).
- Determine which luminescence signal yields ages which are most comparable to validation radiocarbon ages (Nunes, 1999), and apply this method to other similarly aged basalts (Terceira, Hawaii, Tenerife and Gran Canaria).
- Measure palaeo-magnetic intensities on the same samples using the novel pseudo-Thellier method (De Groot, et al., 2013).
- Match obtained palaeo-magnetic intensities with obtained luminescence ages to demonstrate the suitability for OSL dating to constrain PMI data, in areas where radiocarbon is not appropriate or available.

Twenty-two basalt samples from the Island of Pico were focused upon, with its geologically recent volcanic activity and location in the North Atlantic these samples provide an excellent opportunity to view the geologically recent history of the magnetic field and SAMA. The samples were first addressed for their petrology and feldspar mineralogy to support the results. Four other samples from other basaltic islands which already have determined absolute PMI values were also tested with the same luminescence protocols to compare with the results from the Pico samples.

Luminescence dating has been developing since the 1970's, and indicates the time elapsed since a material was last exposed to light or high temperatures (Preusser, et al., 2008). In principle, ionising radiation can excite electrons within a crystal lattice, which may become trapped in lattice defects. As the electrons move back to their lower energy states after light or heat stimulation, they emit a photon signal proportional to the number of trapped electrons, as a function of dose rate. OSL dating has previously been conducted on volcanic feldspars $\geq 12.0 \pm 0.8$ ka by Tsukamoto, et al, (2011) but there is still a need to identify the stable signal components which suitable for dating younger Holocene aged materials.

The Pseudo-Thellier approach was first proposed by Tauxe, et al, (1995) to determine relative palaeo-intensities from carbonate-rich sediments, without the use of a conventional pre-heating stage. The method produces a relative PMI value by normalising a samples Natural Remnant Magnetism (NRM) with an acquired Anhyseretic Remanent Magnetisation (ARM), which is then calibrated to produce an absolute PMI value (Tauxe, et al., 1995). This method was first applied to volcanic samples by De Groot, et al (2013) and the claibration for absolute PMI determination has been refined

over the past few years with expanding data sets from Islands including Hawaii and the Canary Islands (de Groot, et al., 2016 & 2015).

1.2 Geological Setting

The Azores Archipelago is a collection of nine volcanic islands located off the West coast of Portugal, lying on a triple junction between the North American, Nubian and Eurasian plates. To the south lies the South Atlantic Magnetic Anomaly (SAMA), above the Mid-Atlantic Ridge (Figure 1.2.1), where the total geomagnetic field intensity is $\sim 25\mu\text{T}$, compared to the expected value of $43.74\mu\text{T}$ (IGRF, 2014). The proximity of the archipelago to this anomaly is considered ideal for addressing the recent and local magnetic behaviour over the past 3 ka. Pico is the youngest of the islands at 0.27ma (Carine & Schaefer, 2010) and is divided into three main geological provinces (Figure 1.2.1 C): Pico Mountain (youngest), the east-trending fissure system, and the older remnant Topo Lajes volcanic system in the south (Prytulak & Elliott, 2009)

The primary volcanic source magma chamber is considered relatively undeveloped, with little chemical variation between eruptive products over the past 3ka (Miranda, et al., 1998). Bulk

geochemistry data is available from multiple locations around the island, covering all differently-aged lava units (e.g. França, et al, (2006), Nunes, (1999), Prytulak & Elliott, (2009) & Beier, et al., (2012)). The eruptive products are $\sim 78\%$ basalt, $\sim 20\%$ subordinate hawaiites, and only one lava unit found to be compositionally more evolved (Figure 1.2.3) (França, et al., 2006). Geochemical analysis has found feldspar compositions

to range between $\text{An}_{82-31\%}$, with little orthoclase.

There are several palaeomagnetism studies from the neighbouring islands of Sao Miguel and Terceira, using conventional PMI and directional methods. The Island of Sao Miguel recently had PMI measurements for the past 3 ka conducted, presenting two PMI maxima around 600-400BC and 600-800 AD, with a peak intensity of $92.3\mu\text{T}$ (Di Chiara, et al., 2014). Two samples from Terceira dated at 25.7 and 46.3 ka were also measured with a multi-method approach producing total palaeo-intensity values of 24.4 and $24.1\mu\text{T}$ respectively (de Groot, et al., 2016).

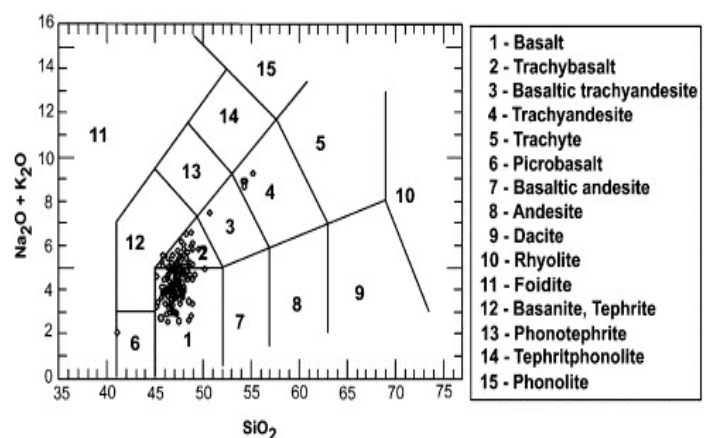


Figure 1.2.1. Classification of volcanic units from the Island of Pico (França, et al., 2006).

1.3 Sample Locations

This research used samples from 22 different lava units collected in 2016 by students at Utrecht University using a water-cooled petrol powered drill (Figure 1.3.1 C & D). At each location, 15-20 cores were taken close together to increase homogeneity between samples. These were divided into two groups- one for OSL measurements, and the other for the PMI and directional measurements conducted here and by BSc students at Utrecht University (Gülcher, (2016), Van Grinsven, (2016) and Wassing, (2016)). Many of the sampled units have already been dated using radiocarbon by Nunes, (1999), obtained from carbon-rich vegetation and debris captured within or below the lava units. Some samples are with age ranges dated as historical flows, and Table 1.3.1 presents a summary of all study locations radiocarbon ages and what methods the samples were tested with.

Individual samples from the islands of Hawaii, Tenerife, Gran Canaria and Terceira (Azores) were also provided from storage at Utrecht University. These samples were all also classified as mafic, ranging from basalts to trachytes. Terceira is believed to be geochemically similar to Pico, with plagioclases dominant, with An46-50% (Calvert, et al., 2006). The Tenerife and Gran Canaria samples are mainly alkali feldspars such as anorthoclase (McDougall & Schmincke, 1976), and the sample from Hawaii is also plagioclase rich (Calvert, et al., 2006).

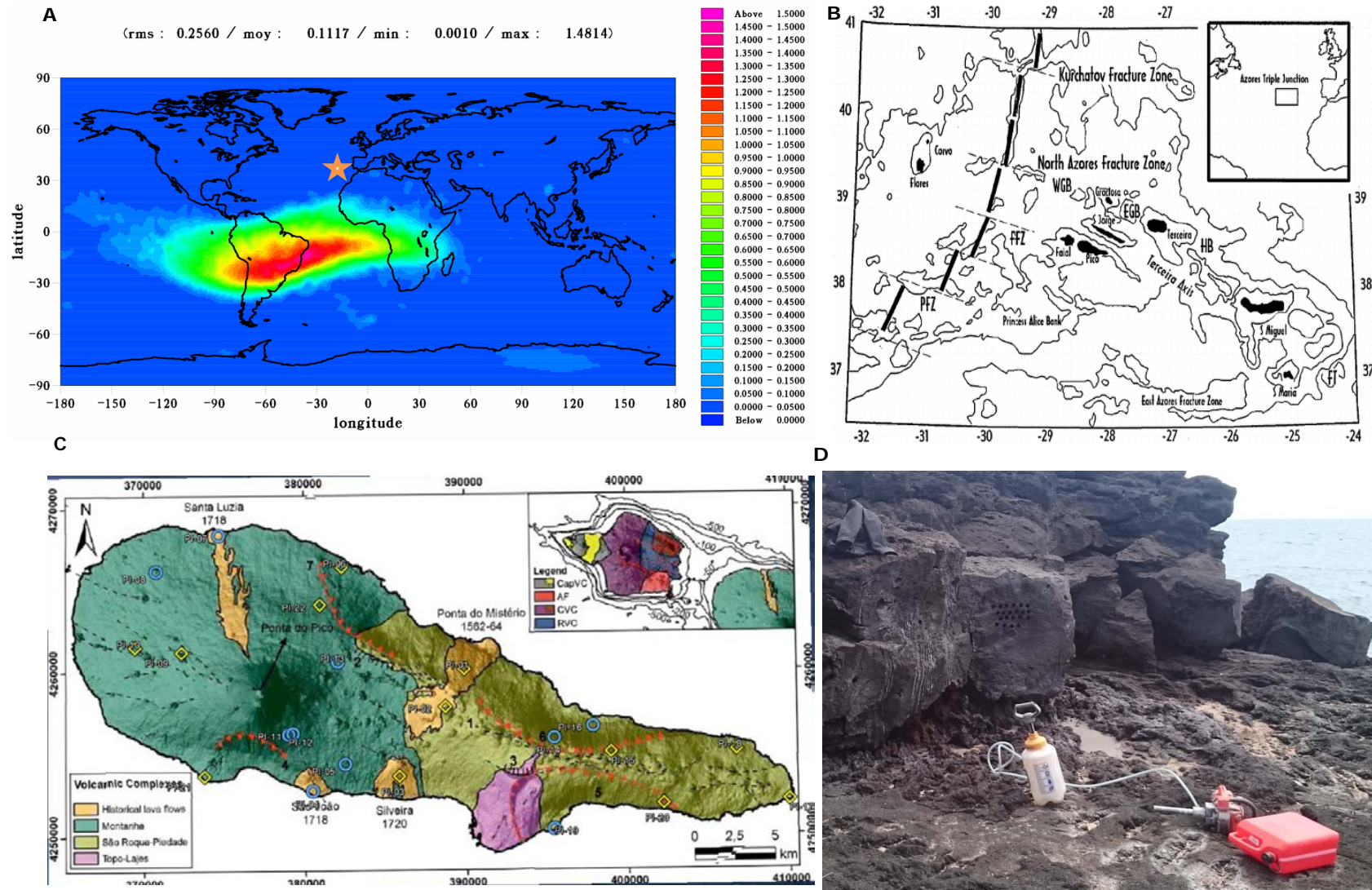


Figure 1.3.1. A) Location of the South Atlantic Anomaly, and proximity to the Azores (star) (Lemoine & Capdeville, 2006). B) Sketch of Azores located on the Azores triple junction, and proximity to Terceira (Miranda, et al., 1998). C) Map of main volcanic units modified from Quartau, et al., (2015) with all Pico sample locations. Yellow diamonds are the ones selected for luminescence dating. D) Sampling method used by BSc students at Utrecht University.

Sample ID	Island	Coordinates	¹⁴C Age Bp	Mean Calibrated ¹⁴C Age	1σ intervals, & relative probabilities	Reference	Application
PI-01	Pico	38.483, -28.263	453±1	1563 (AD)		Historical Flow	pTh
PI-02	Pico	38.462, -28.276	453±1	1563 (AD)		Historical Flow	pTh
PI-03	Pico	38.423, -28.308	296	1720 (AD)		Historical Flow	pTh
PI-04	Pico	38.414, -28.370	298	1718 (AD)		Historical Flow	M&P, OSL, pTh
PI-05	Pico	38.412, -28.346	625 ±65	1346 (AD)	1292-1328 (0.392), 1341-1395 (0.608)	(Nunes, 1999)	M&P, OSL, pTh
PI-06	Pico	38.539, -28.350	1725±55	310 (AD)	252-305 (0.437), 311-383 (0.563)	(Nunes, 1999)	pTh
PI-07	Pico	38.556, -28.439		1720(AD)		Historical Flow	M&P, OSL, pTh
PI-08	Pico	38.536, -28.482	1615±40	453 (AD)	394-434 (0.442). 455-469 (0.106)		M&P, OSL, pTh
PI-09	Pico	38.491, -28.462	1390±70	641 (AD)	575-687 (1.000)	(Nunes, 1999)	pTh
PI-10	Pico	38.494, -28.496	500-1000	1000-1300(AD) (1300 AD)			pTh
PI-11	Pico	38.447, -28.383	1310±70	719 (AD)	652-771 (1.000)	(Nunes, 1999)	M&P, OSL, pTh
PI-12	Pico	38.446, -28.386	1670±115	368 (AD)	244-436 (0.756). 446-472 (0.08)	(Nunes, 1999)	M&P, OSL, pTh
PI-13	Pico	38.486, -28.352	365±75	1543 (AD)	1453-1524 (0.502), 1558-1631 (0.498)	(Nunes, 1999)	M&P, OSL, pTh
PI-14	Pico	38.446, -28.200	2720±50	-873(AD)	905-820 (1.000)	(Nunes, 1999)	M&P, OSL, pTh
PI-15	Pico	38.439, -28.161	1405±50	630 (AD)	602-663 (1.000)	(Nunes, 1999)	pTh
PI-16	Pico	38.452, -28.172	1105±45	934 (AD)	893-986 (1.000)	(Nunes, 1999)	M&P, OSL, pTh
PI-17	Pico	38.412, -28.032	1780±70	247 (AD)	140-160 (0.099), 165-196 (0.158), 208-333 (0.742)	(Nunes, 1999)	pTh
PI-18	Pico	38.440, -28.070	1780±70	247 (AD)	140-160 (0.099), 165-196 (0.158), 208-333 (0.742)	(Nunes, 1999)	pTh
PI-19	Pico	38.395, -28.199	3520±60	-1844 (AD)	1921-1762 (1.000)	(Nunes, 1999)	M&P, OSL, pTh
PI-20	Pico	38.410, -28.122	2000-	-6000-0 (AD)			pTh

PI-21	Pico	38.423, -28.447	10,000	(0 AD)				pTh
PI-22	Pico	38.518, -28.366	1500-5000	-3000-500 (AD)				pTh
HW-10	Hawaii	19.636, -155.049	1470 ± 50	588 (AD)	558-640 (1.000)		(De Groot, et al., 2013)	OSL
TER-18	Terceira	38.790, -27.195	1760 ± 40	283 (AD)	141-160 (0.031), 165-196 (0.058), 209-384 (0.911)		(de Groot, et al., 2016)	OSL
GCR-47	Gran Canaria	28.064, -15.662	3030 ± 90	1266 (BC)	1406-1191 (0.912), 1176-1163 (0.043), 1144-1131 (0.046)		(de Groot, et al., 2015)	OSL
TF-6	Tenerife	28.248, -16.707	3620 ± 140	1995 (BC)	2196-2169 (0.057), 2148-1865 (0.780), 1849-1773 (0.163)		(de Groot, et al., 2015)	OSL

Table 1.3.1. Summary of all sample locations, with coordinates, radiocarbon and calibrated ages, with corresponding 1σ probability intervals. Source references for the radiocarbon ages are given, along with what the samples were used for in this study. Ages in brackets are the minimum ages used for data presentation.

2. Petrology and Mineralogy

2.1 Introduction

Using the feldspar, quartz and Fe-Ti-oxides from basalt, these minerals were compositionally addressed to determine their suitability for the main methods presented here.

Feldspars are aluminosilicate minerals generally classified into 2 groups. The plagioclase feldspars form a solid solution series between Na- and Ca-rich end members Albite and Anorthite, and the alkali feldspars also have a solid solution between K- and Na- rich endmembers Orthoclase and Albite. According to Bowen's reaction series (Figure 2.1.1) at higher temperatures Ca is dominant, and as temperatures decrease, Na and K are found substituting Ca. Potassium rich feldspars are favoured for luminescence measurements, as the internal K content provides a higher irradiation dose, which increases the internal dose rate and can circumvent problems of disequilibria in the external contributing radioactive isotopes. Sodium rich endmembers are also found to be suitable for luminescence dating as they can also give bright emissions. The Ca-rich endmembers are less well explored, but are generally less favoured for luminescence as it has been found that anomalous fading increases with increasing Ca content (Panzeri, et al., 2012), increasing age

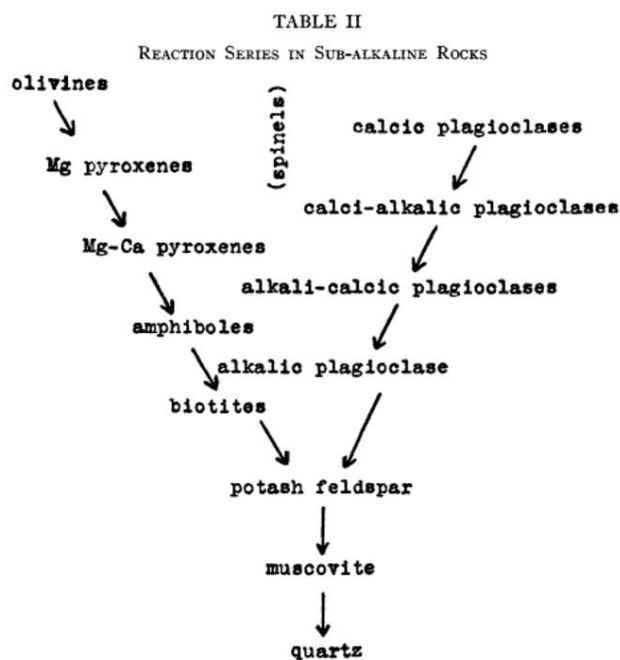


Figure 2.1.1 Bowen's reaction series, with decreasing temperatures and increasing SiO₂ in the directions of the arrows. (Bowen, 1922)

underestimations in the results. Exploration using a polarising microscope and a scanning electron microscope (SEM) with Energy Dispersed Spectroscopy (EDS) enabled an insight into the basalt mineral assemblages, abundances and compositions opening room for discussions of the OSL results which they influence.

To measure and understand the results from PMI tests, it is important to know what is providing the magnetic remanence in the basalt samples. The magnetic intensity (B, μ T) can only be captured and stored if the properties of the mineral (e.g. oxidation state) are suitable to replicate the field and store it in a way which minimises the total energy, with different states with different properties, often relating to grain size.

Fe-Ti-oxides such as magnetite and hematite have been the focus of most palaeo-magnetism studies. These minerals form from a solid solution series between rutile (TiO_2), wüstite (FeO) and hematite (Fe_2O_3) (Figure 2.1.2) (Lowrie, 2007), which governs the magnetic behaviour. The electron configurations controlling the magnetic moments are- to a degree- a function of crystal size. The simplest electron configuration produces single-domain (SD) particles, with the electron spins (anti-) parallel to each other in small grains. As the crystals get bigger, magnetic domains divide with energy being minimised by spins diverging from the strict parallel structure. These Multi-Domain (MD)

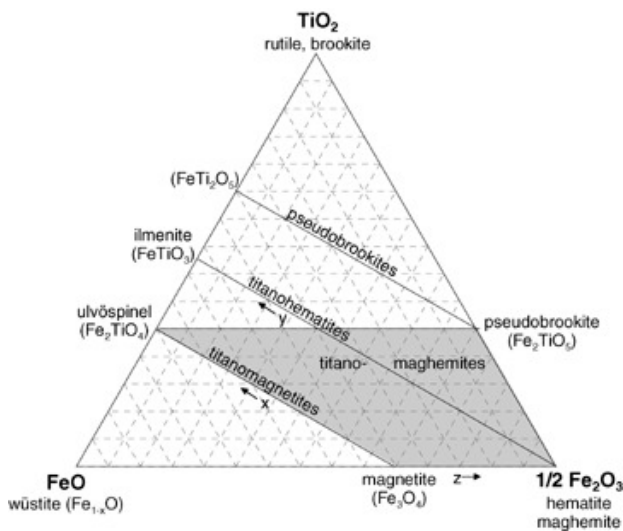


Figure 2.1.2 Ternary plot of Fe-Ti-Oxides (Franke, et al., 2007).

grains have lower coercivity¹ and remanence² than SD grains. Most rocks contain a mixture of SD and MD grains, leading to Pseudo-Single Domain (PSD) properties with a mix of domain properties. In PMI studies, it is favourable to have SD or PSD minerals within your sample, to increase accuracy and precision. The nature of the magnetic minerals can be explored using an SEM and EDS, as well as a vibrating sample magnetometer (VSM) which gives information on domain states. Together these results will form a backing for the interpretation and discussion of the luminescence and pseudo-Thellier results.

2.2 Theoretical background

Here, a brief explanation of the methods used here for the mineralogical and petrological assessments is given.

Michel-Levy

The Michel Levy method for plagioclase feldspar composition determination (Nesse, 2000) utilises a minerals' known extinction angles and maximum birefringence to indicate the abundances of Na (Albite) and Ca (Anorthite) in sub- to euhedral twinned plagioclase, using thin sections and a polarising microscope. Assessment of the fast and slow ray indicates whether the mineral is Na or Ca rich, and thus which contour line to address for the An% using Figure 2.2.1. Only an estimate of the An% can be made, with no assessment of the K content. This method was used here as a preliminary assessment of the types of feldspars which were being measured with the OSL.

¹ Resistance of the magnetic characteristics to change.

² Magnetisation remaining in the mineral once an external magnetic field is removed

SEM and EDS

The development of the Scanning Electron Microscope has enabled the high-resolution imaging and assessment of organic and inorganic materials and minerals. Using a fine focused beam of electrons, a point location or section of the material produces a signal such as one of backscattered electrons which highlights topography of the material (Goldstein, et al., 2012). With the

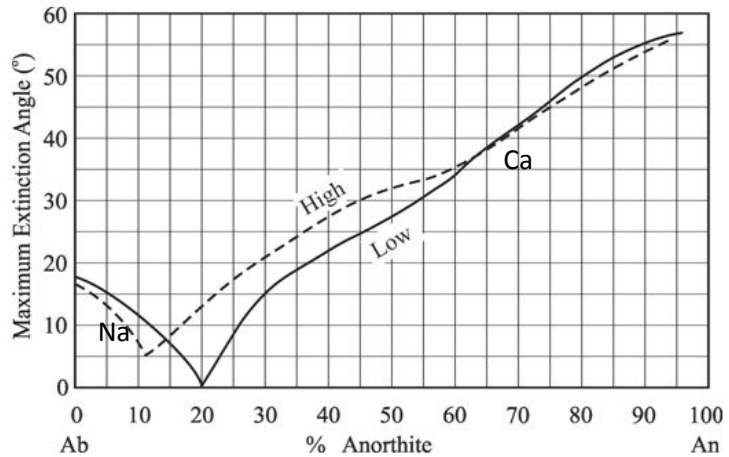


Figure 2.2.1 Graph used with Michel-Levy measurements to determine the abundance of Na and Ca. Dotted line is to be used with volcanic samples, and the solid line is for use with plutonic samples. (Nesse, 2000).

addition of an Energy Dispersive spectroscopy (EDS) attachment, minerals are able to be assessed for their relative elemental abundances. A beam of electrons interacts with the surface of the mineral or material, and the response of the electrons provides information on the electron configurations. The EDS can provide information on oxide contents in mass% or compound mass%.

VSM

The Vibrating sample magnetometer (VSM) enables assessment of the magnetic domains used in palaeomagnetism studies. It is often used prior to pTh measurements to help assess the suitability and stability of the magnetic minerals for PMI determination. This high-field method uses fields up to 1.5T to determine hysteresis properties which are summarised in a Day plot (Figure 2.2.2) (Day, et al., 1977), which shows magnetic domain properties as a function of grain size, and - to a lesser extent- compositional mixing. A sample is placed between two magnets, vibrated and subjected to a high calibrated electromagnetic field. First, the sample is fully magnetised in a positive direction, then the field is reduced to zero, reversed and then magnetised in the same stepwise manner in a negative direction, completing a hysteresis loop (Figure 2.2.3 A). The physical oscillations between the magnets during the de- and re-magnetisation induce a voltage which is proportional to the magnetic moments of the minerals (Collinson, 2013). The magnetisation is plotted as a function of applied field, and using the hysteresis plot, the domain structure of the magnetic oxides can be determined, with the magnetic saturation (MS, maximum level of magnetisation), remnant magnetism (Mr, permanent natural magnetism) and coercive field (HC, field at which the remanence is annulled) values obtained.

A second high-field test creates a Direct Current demagnetisation (DCD) curve (Figure 2.2.3 B) and is used to assess the behaviour of the magnetic moments after the application of an external field. This curves calculates the remnant coercivity (HCR) which is the natural coercivity at time of the mineral passing below its respective curie temperature. From magnetic saturation at 1.5T, the

sample is demagnetised in a step wise manner. The magnetisation is plotted over field strength, and the HCR value is at 0mT.

Taking these values, a Day plot is created, plotting the ratios M_r/M_s over H_{cr}/H_c (Figure 2.2.2). Established boundaries define where the SD, PSD and MD mineral characteristics lie, and along which mixing path the magnetite crystals formed (Dunlop, 2002).

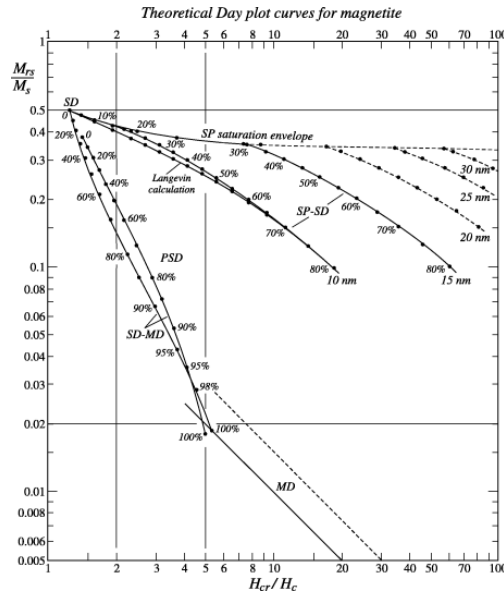


Figure 2.2.3 . Example of a Day plot from (Dunlop, 2002) with domain boundaries defined and theoretical mixing curves for magnetite as they crystallise.

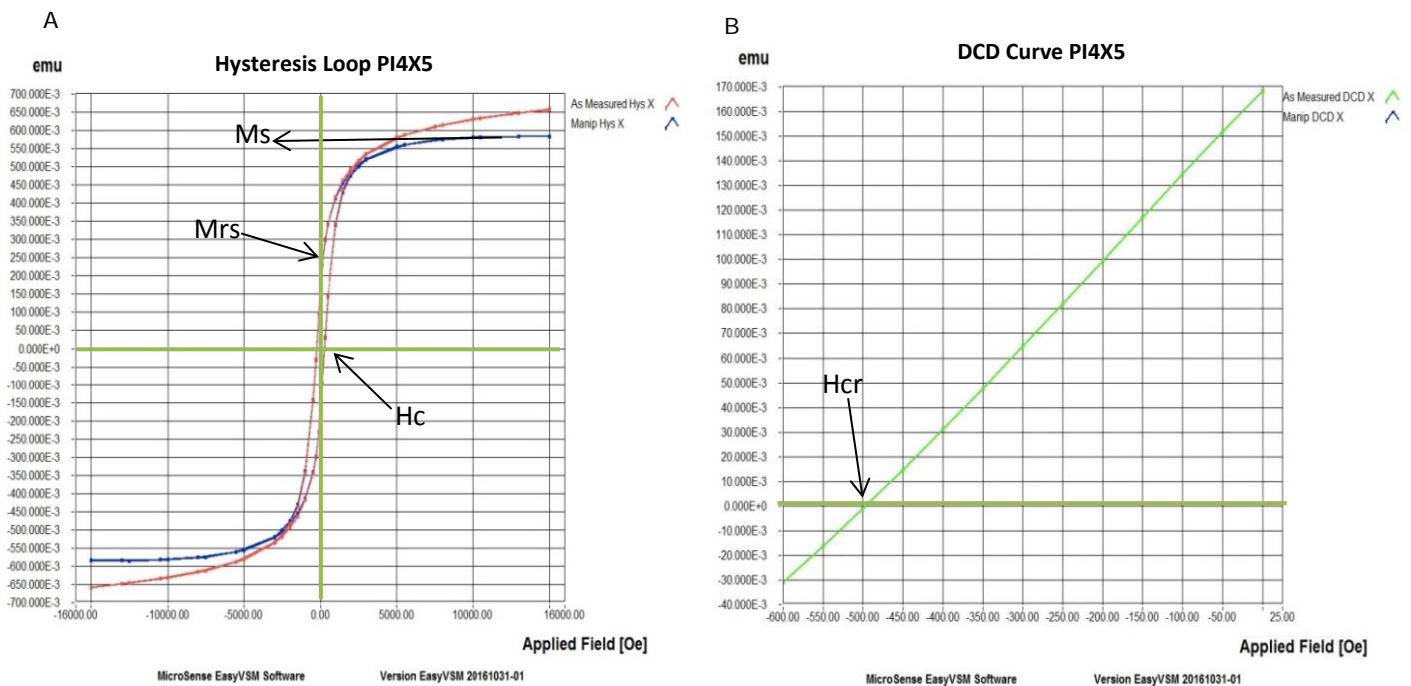


Figure 2.2.2 A) example of a hysteresis plot, with the demagnetisation and re-magnetisation curves plotted and H_c (field coercivity), M_{rs} (remnant magnetic saturation) and M_s (magnetic saturation) values obtained. And B) DCD curve, with the H_{cr} (remnant coercivity) value obtained as it crosses the X axis.

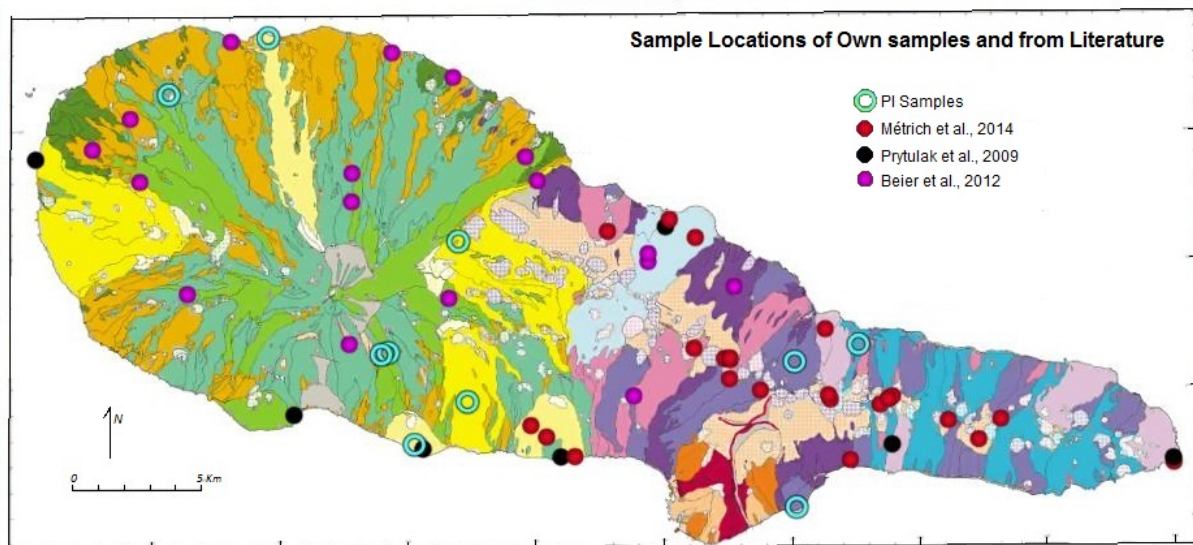
2.3 Applied Methodology

Thin sections of the 10 Pico samples selected for the OSL measurements were visually assessed for mineral constituents, grain sizes, structures and textures, using a Leica polarising microscope at Utrecht University. Digital images were taken of the samples and estimations of the mineral constituent percentages were made. Using the Michel-Lévy method (Nesse, 2000) preliminary compositions of feldspar phenocrysts were determined in samples PI-07, -12 and -19, as these were the focus for the OSL dating. As validation for the Michel-Lévy results, the thin sections were carbon coated and a table-top SEM with EDS was used to measure the relative chemical compositions of the feldspars and magnetic minerals (K, Ca, Na, Fe, Ti and Al). An attempt was made to use point measurements on the same feldspars as were measured with the Michel-Lévy method, gathering data for the phenocrysts considered as the primary luminescence centres, as well as magnetic minerals. Information on internal potassium content was used for determining internal dose rates. Insufficient time was available to measure minerals in all samples.

To calculate luminescence ages, information on total dose rates (D_R) from ionising radiation within the rock sample is needed. Preliminary total U, Th and K D_R values for the 10 OSL Pico samples were calculated using bulk geochemistry data from literature (Prytulak & Elliott, (2009), Métrich, (2014) and Beier, et al., (2012)). The study locations from the literature were plotted in Google Earth, with a geological map of Pico overlay (Figure 2.3.1, and corresponding table). A visual pairing based on geological unit and unit ages was conducted, of all sample locations and the specific U, Th and K ppm values were selected.

The internal K mass% values from the EDS tests were used for appropriate samples. The samples which did not have their internal chemistries measured were paired with a similarly aged Pico sample which was measured, calculated with the 4-11 μ m grain size fraction, and 2 \pm 2% water content as low connectivity and infiltration was assumed within the lava units. Grain size and water content attenuation factors were also accounted for.

Here, the samples were prepared in the Nederlands Centrum voor Luminescentiedatering (NCL) laboratory at Wageningen University and Research centre. A precision saw and diamond drill piece were used to trim the outer light-bleached material for dose rate (D_R) determination, and create 8mm diameter cores for palaeodose (D_e) determination. The D_R material was crushed to <300 μ m, mixed with melted wax in a 0.7: 0.3g ratio and made into 2cm thick 'pucks'. The bulk ionising radiation was then measured for 22 hours using low-level gamma spectroscopy at the Rikilt Laboratory at Wageningen UR. Only samples PI-07, -12, -19, HW-10, TF-6, GCR-47 and TER-18 were measured as these were of interest in this study.



Pico Sample	Literature sample
PI04	PI-11, Prytulak et al., 2009
PI07	AZP-03-45, Beier, et al., 2012
PI13	AZP-03-01, Beier et al., 2012
PI05	AZP-03-47, Beier et al., 2012
PI16	PIC- 30, Métrich et al., 2014
PI11	AZP-03-47, Beier et al., 2012
PI08	AZP-03-45, Beier et al., 2012
PI12	P25, Beier et al., 2012
PI14	PIC- 31, Métrich et al., 2014
PI19	PIC- 37, Métrich et al., 2014

Figure 2.3.1. Geological map with literature and own sample locations used for literature dose rate determination. Left: Table with paired own and literature samples.

Magnetic Domain properties for all 22 Pico samples were measured using a VSM at Utrecht University. Hysteresis curves for 1 sample from each of the 22 Pico locations were created. The samples were subject to high fields up to 1.5mT. The hysteresis loop provided values for the magnetic saturation³, remnant magnetism⁴ and coercive field⁵. Direct Current Demagnetisation (DCD) curves were then created for each sample and the remnant coercivity⁶ was obtained. These

values were plotted in a Day plot to provide information on the magnetic domains of the minerals providing the primary magnetic signatures.

³ Ms, maximum magnetisation which the mineral can retain, emu.

⁴ Mr, residual magnetism remaining after removal of an external field, emu.

⁵ Hc, strength of field necessary to completely demagnetise a sample, Oe.

⁶ Hrc, coercivity at time of primary magnetisation, Oe.

2.4 Results

Microscopy

Thin section analysis of the 10 Pico basalts showed that all samples had similar groundmasses of olivine, clino-pyroxene, plagioclase, and opaque magnetic minerals. The coarseness of the groundmass varied, with the younger samples generally having finer grain sizes (<0.5mm). Phenocrysts of olivine and clinopyroxene were present in all, but phenocrysts of plagioclase were only present in samples PI-07, -11, -12, -14, and -19, all ≤ 6 mm in length (Figure 2.4.1). None of the samples showed evidence of mineral alteration, and all phenocrysts were sub- to euhedral. On average for all samples, groundmasses were estimated to have ~42.5% feldspar and ~18% magnetic minerals, with an estimated average of ~37% feldspar phenocrysts. Table A2.4.1 in the appendix summarises the estimated percentage of the mineral constituents and crystal size fractions.

Many of the feldspar phenocrysts were not suitable to conduct the Michel-Levy measurements with some crystals showing zoning (Figure 2.4.1 C). The results of the successful measurements are shown in a ternary diagram (Figure 2.4.2 A) plotted using Tri-plot v1.4.2 workbook (Graham & Midgley, 2000). There was some compositional variation between the phenocrysts, and was most noticeable in PI-07 where the Anorthite % ranged from 3 to 50.5 An%. PI-12 had all Na rich feldspars and PI-19 had a slight mixture averaging around 45.25 An%. Full results of the Michel-Levy tests and a summary of the visual assessments are presented in the Appendix.

SEM and EDS

Several phenocrysts addressed with the Leica microscope were successfully located with the SEM and EDS (Figure 2.4.3). The Ca, Na and K mass percentages from the EDS were normalised and displayed in a ternary plot (Figure 2.4.2 B). The Michel-Levy results generally underestimated the Ca content, with the EDS results showing both the feldspar groundmass and phenocryst phases were all Bytownite – Labradorite with >50 An%, and little compositional variety. The highest K contents were found in samples PI-07 and PI-12 with a peak value normalised to 3.72% from sample PI-07. However, this sample also had the lowest K abundance at 0.52%. Samples PI-12 and -07 also had the highest Na values, with again PI-07 producing the largest range in Na from 2.3-35.31 mass %.

Only 3 magnetic minerals were measured without the results suffering incredibly high measurement errors. Sample PI-04 and PI-11 were dominant in FeO, with compound mass % of 54.78 and 55.52 respectively. PI-16 had a mixture with 49.97 TiO₂ mass% and 49.25 FeO mass% and possibly be classified as Ilmenite, although further measurements would be beneficial to do.

Table A2.4.3 in the appendix summarises all elemental mass% values received from the EDS, and Figure A2.4.1 shows ternary plots of individual plagioclase sample results.



Figure 2.4.1 Examples of images from the Leica Polarising microscope. Left: Plain polarised light, right: crossed polarised light. A) PI-08 lacking significant phenocryst phases, with abundant magnetic minerals. B) PI-04 with only olivine and pyroxene phenocrysts and a coarse feldspar-rich groundmass. C) PI-19 with large plagioclase phenocrysts and a coarse groundmass (>0.5mm). Pl: plagioclase, Ol: olivine, Opq: opaque minerals, Ilm: Ilmenite, Cpx: clinopyroxene.

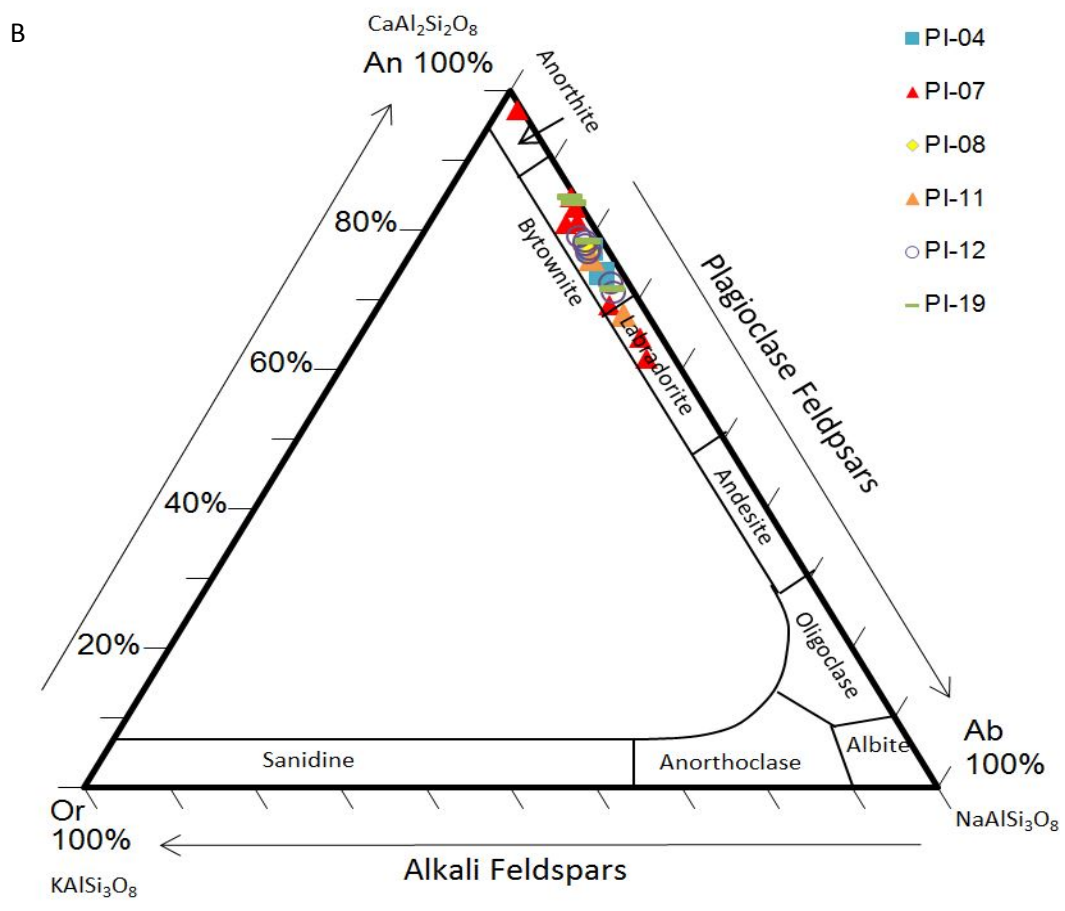
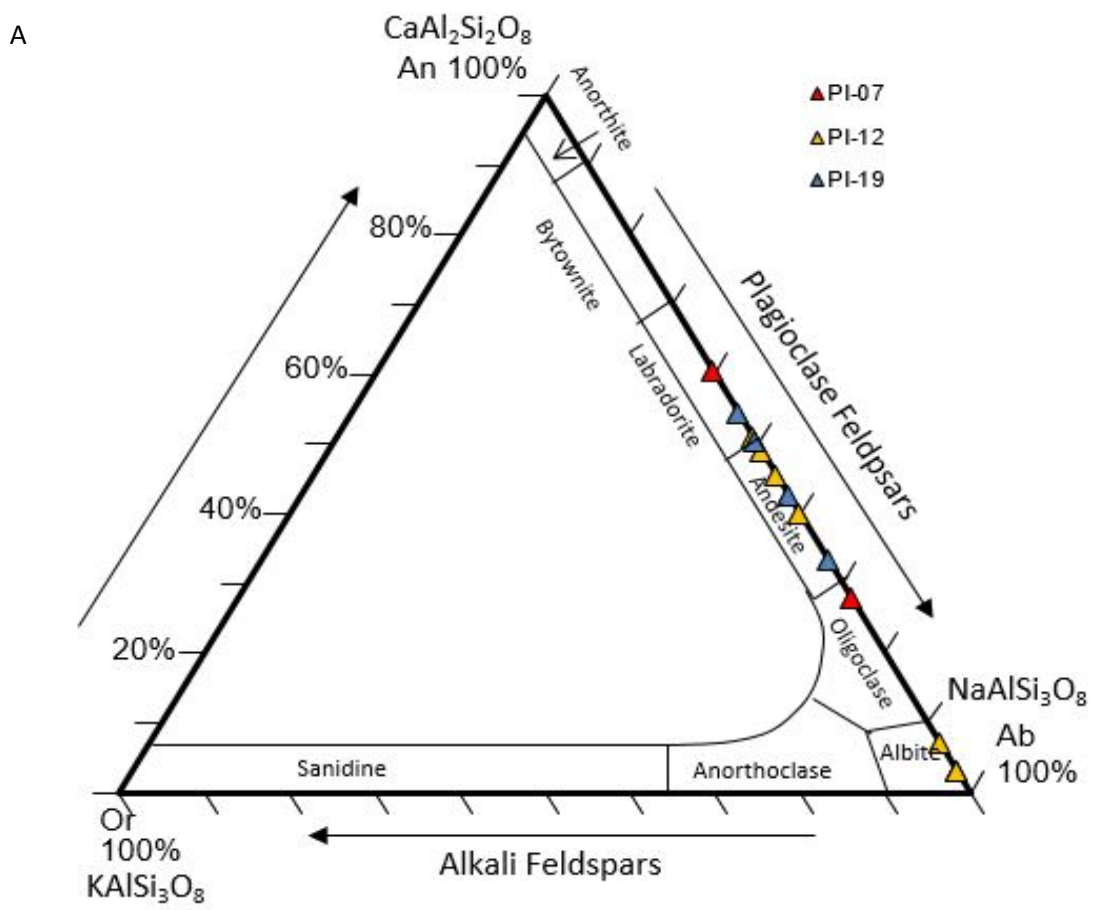


Figure 2.4.2 A) Ternary plot of Michel-Levy results from measured phenocrysts in samples PI-07, -12 and -19. Points are plotted on the Ab-An axis as Or% is not known. B) Ternary plot of all EDS results, with all measured plagioclases >50An%.

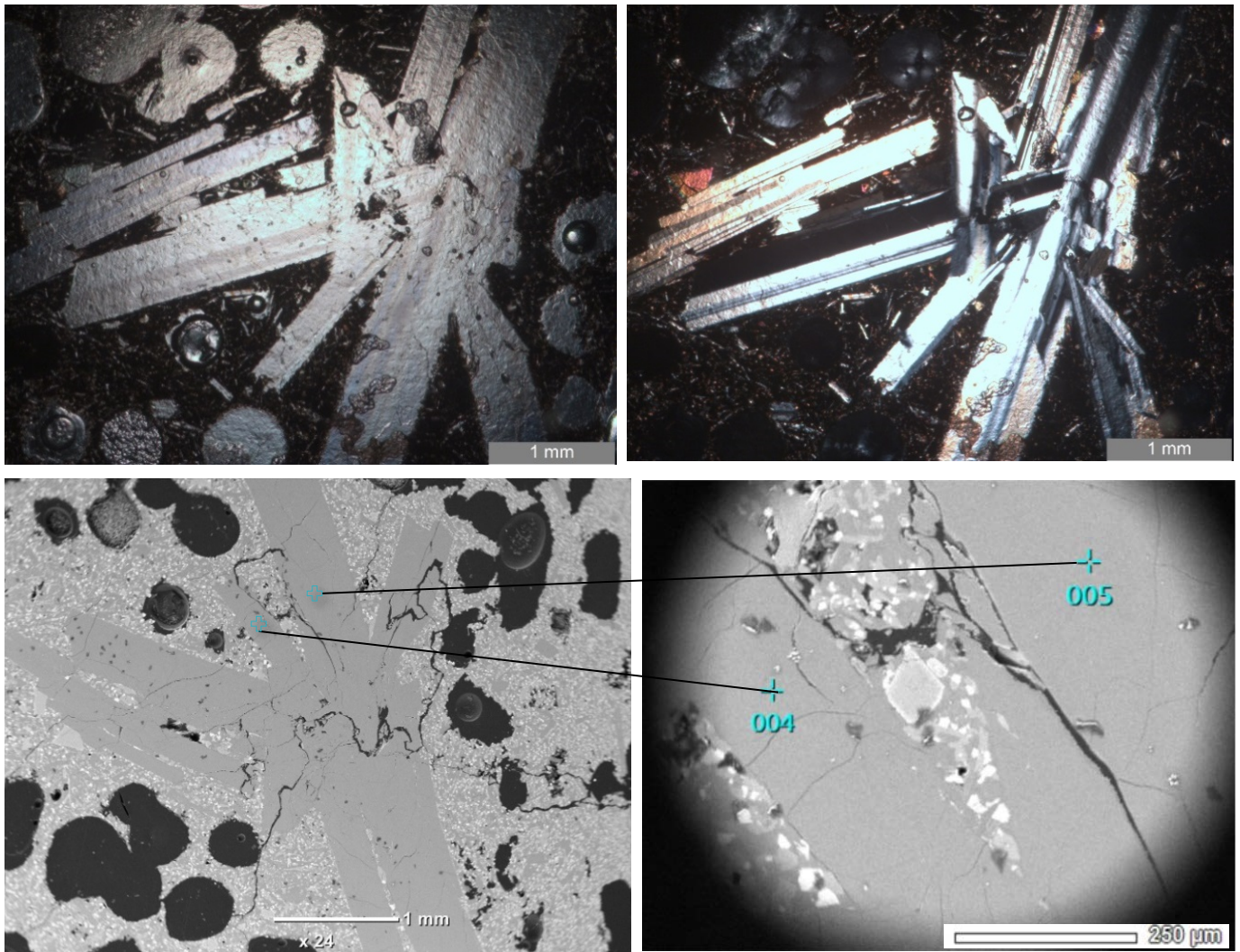


Figure 2.4.3 Matching of Leica (left: plain polarised light, right: crossed polars) and SEM/EDS measurements, an example of a plagioclase crystal patch from sample PI-12, and the point measurements which were taken.

Dose rate determination

The potassium mass percentage values from the EDS were used for literature D_R calculation. The average total literature dose rate from all ten Pico samples amounted to 2.62 ± 0.62 Gy/ka, with the highest from PI-14 at 3.51 ± 0.07 Gy/ka, and the lowest from PI-13 at 1.51 ± 0.14 Gy/ka. Full results are available in the appendix. The measured D_R values for PI-07, -12 and -19 were calculated for the 4-11 μm fraction as these were the focus of the OSL tests, as well as dose rates for the four other samples (HW-10, TER-18, GCR-47 and TF-6). The measured dose rates range from 1.76 to 5.87 Gy/ka for the 4-11 μm fraction.

The results from the other four basalts were very variable, with the sample from Terceira producing the highest value at 5.77 ± 0.20 Gy/ka. Sample HW-10 was not able to be measured, with too low counts registered within 22 hours. Table 2.4.1 summarises the results, and full measured results are found in Table A2.4.5 in the appendix.

Sample	Literature DR (Gy/ka)	Measured DR (Gy/ka) 4-11 μ m
PI-07	3.11 \pm 0.34	2.13 \pm 0.08
PI-12	2.07 \pm 0.20	2.08 \pm 0.08
PI-19	2.27 \pm 0.05	1.76 \pm 0.07
HW-10		Too low counts
TER-18		5.77 \pm 0.20
GCR-47		2.38 \pm 0.09
TF-6		3.76 \pm 0.13

Table 2.4.1. Summary of Literature and measured dose rates for the 4-11 μ m fraction.

VSM

The results of the VSM show all samples have pseudo-single domain (PSD) properties (Figure 2.4.4), clustering relatively close to the single domain classification. The average remnant coercivity (H_{rc}) is 340.70 Oe, much larger than the average coercive field (H_c) at 164.91 Oe, indicating the mineral coercivities have most likely been stable over time. Only one sample (PI4X5) had a significantly higher H_{rc}/H_r value (8.05) and a less stable MD character. Sample PI11X5 also deviates from the cluster of other sample points, having the lowest M_{rs}/M_s ratio at 0.07. The average remnant magnetic saturation (M_{rs}) lies at 0.07 emu, significantly smaller than the average magnetic saturation (M_s) at 0.41emu. Full results of the Hysteresis and DCD plots are found in appendix Table A.2.4.6.

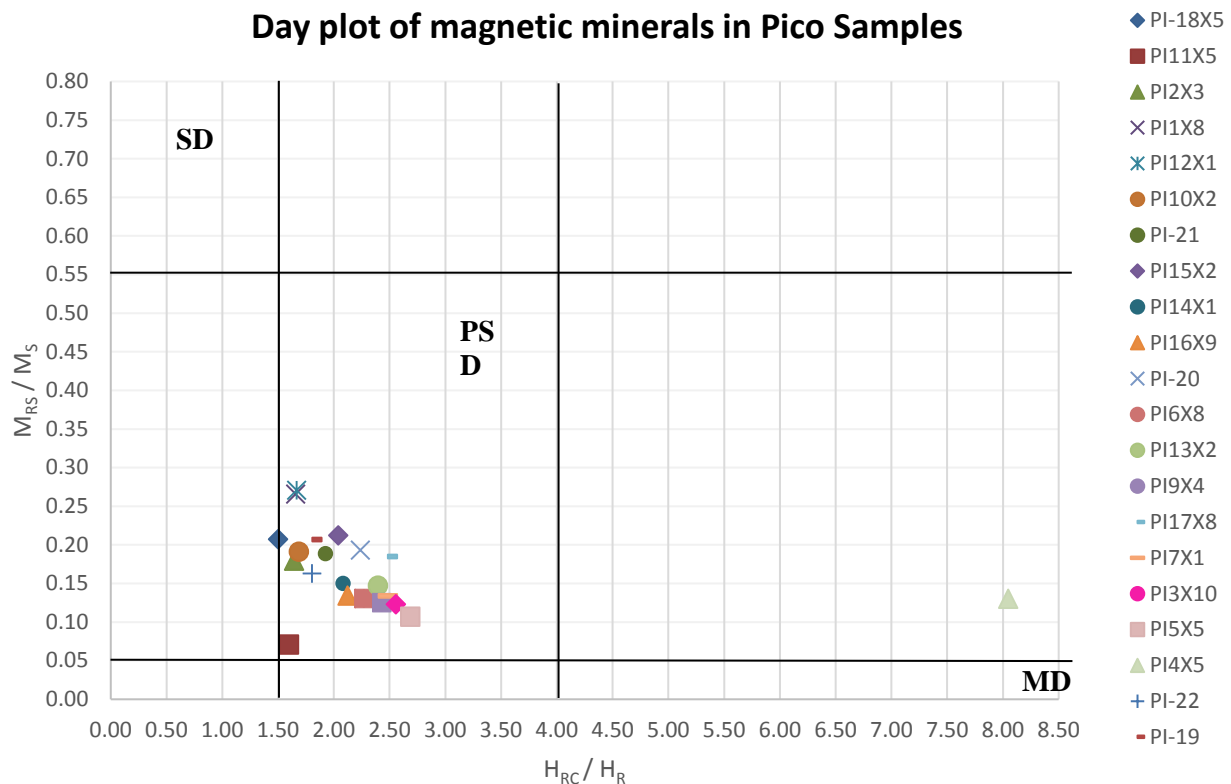


Figure 2.4.4 Day plot displaying domain properties from the VSM of measured magnetic minerals. Domain boundaries are taken from (Day, et al., 1977). All results fall on a mixing curve of SD and MD grains, indicating a mix of small- medium grain sizes

2.5 Discussion

From analysis of the thin sections, all samples were compositionally similar, with variations only being in grain sizes and abundance of feldspar phenocrysts. Estimating the compositions using the Michel-Levy method appeared to have been biased, with underestimations of calcium content in all measurements, compared to the results of the EDS. The Michel-Levy method relies on well-formed lamellae and the presence of sufficiently large crystals to measure. This introduces unquantifiable measurement bias as only the largest and most euhedral plagioclase phenocrysts were selected for measurement and here, with measurements only taken on PI-07, -12 and -19, the results are not representative of any heterogeneity within or between lava units.

From the SEM/EDS results all 10 Pico samples showed similar feldspar compositions, dominated by Ca over Na or K. The high Ca-contents indicated that obtaining stable luminescence signals from these samples was most likely going to be difficult due to the increased chance of high anomalous fading rates due to the high calcium and low potassium. The compositional results are consistent with those found in literature, with high Anorthite compositions (França, et al., 2006). The compositional consistency between the different lava units supports the idea of a young and undeveloped magma source, feeding the Island volcanism (França, et al., 2006). Sample PI-07 had the largest compositional variation, with the largest ranges of Ca, Na and K mass percentages. The reason for this is unknown, but may be due to magma mixing of 2 or more components or the presence of xenocrysts or rock fragments from past eruptions, which have been found in this unit (Mitchell, et al., 2008).

Comparing the literature and measured D_R values, the literature values produced a bias towards higher doses, with the measured values lower than the literature D_R values. This may be because of differences in sample preparation and measurement methods, but the literature values were only used for gaining an idea on the expected dose rates and are not discussed further. The results from the other four samples were very variable, with no result from HW-10, which could indicate the source of the lava is depleted in radioactive elements, or the measurement period of 22 hours was just not sufficient. There was not enough time to re-measure this sample. The very high value from TER-18 is also surprising being from the neighbouring Island of Terceira, it was expected that there would be consistency between this and the Pico samples. The systematic measurement errors of the D_R measurements are at 7%, with random errors at 3% and automatically accounted for in the D_R calculation.

Visual assessments found samples PI-11 and -16 contained the most abundant magnetic opaque minerals, contributing an estimated 30% of the groundmasses. From the Day plot, only PI-11

shows any possible influence of this, with a relatively lower saturation than the rest of the samples possibly due to the size of the minerals being larger.

With only 3 successful EDS measurements taken on magnetic minerals, conclusions are hard to make as they are not representative, although the minerals are assumed to be low-medium Ti-magnetite's and Ilmenites, considering the EDS results. Other studies have found these are common as inclusions within other minerals, and often present in high temperature ($>500^{\circ}\text{C}$) Mid-Ocean Ridge Basalts (MORB) (Wang & Van der Voo, 2004), so it is plausible that they are present here. It has been established that with decreasing Ti content, the curie temperature and spontaneous magnetisation increase (Lowrie, 2007). Samples PI-04 and PI-11 – with their high Fe abundances compared to PI-16 – possibly have high curie temperatures and are therefore unlikely to have undergone re-magnetisation due to re-heating of the lava unit by overlying deposits. However, it is hard to support this statement with such an under-representative sample number.

The results of the VSM and hysteresis measurements indicate that the samples are generally suitable for producing reliable results from the pTh measurements. As most the samples show pseudo-single domain properties (with a mixture of single and multiple domain minerals possibly as a product of different grain sizes). The magnetic minerals have relatively high coercivities and low magnetic susceptibilities, meaning they are unlikely to have been thermally or chemically altered or re-magnetised prior to measurement, enabling measurement of the primary NRM.

3. Luminescence

3.1 Introduction

Since the 1970's luminescence from materials such as sedimentary and volcanic quartz and feldspar has been measured and used for determining the time elapsed since last exposure to light at different wavelengths or high temperatures (e.g. basalt eruption temperatures $>700^{\circ}\text{C}$ (Fattahi & Stokes, 2003)). When a natural crystal is exposed to environmental ionising radiation, electrons can become excited and become trapped in crystal defects and impurities instead of recombining to their original lower energy states. The number of trapped electrons increases with time as a function of the environmental dose rate and the photon emission from the electrons emitted as they recombine can be used to calculate the time elapsed since the samples luminescence signal was last zeroed by exposure to light or heat.

Exploration into feldspar luminescence began using thermo-luminescence (TL) on feldspars from sedimentary and volcanic sources (Wintle, 1977). Recent works have been successful at characterising the decay components within sodic and alkali feldspars, and achieving upper datable limits of 500-600ka (Chen, et al., 2015), and lower age limits of a few decades (Wintle, 2008). Typical K-feldspar TL and optically stimulated (OSL) decay curves are seen in Figure 3.1.1 (Ademola, 2014), with a bright TL peak, and a fast decay curve from IRSL stimulation with high counts.

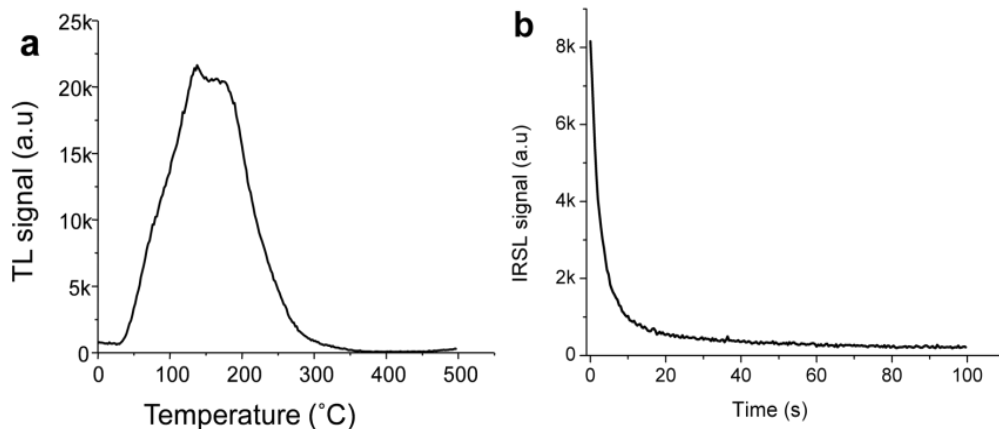


Figure 3.1.1 Examples of A) Thermoluminescence peak, and B) IRSL decay curve taken at room temperature from a pegmatite-sourced K-feldspar (Ademola, 2014).

Using feldspars for luminescence dating has been problematic as it was found that the emission can spontaneously decrease over time. This loss of signal was termed anomalous fading and is observed at room temperatures (Wintle, 1977), can lead to age underestimates and requires measuring the fading rates and application of an age correction factor (g-value) (Auclair, et al., 2003). Recent arguments promote that the fading is caused by quantum mechanical tunnelling, where the electrons tunnel from their principal traps, until they recombine at their nearest recombination centres (Huntley, 2006). Despite these problems, the benefits of using feldspars outweigh the negatives, with

To calculate the time since a luminescence signal was zeroed, information on the total amount of absorbed energy per mass of mineral from the natural ionising irradiation must be obtained to determine the palaeo-dose (D_e). This is achieved by comparing the natural luminescence signal (L_n) from a sample to an artificially induced signal produced by a known irradiation dose (L_x). The sample is artificially irradiated with at least 3 increasing regenerative doses, stimulating with either a heat plate under the aliquot, or by a LED after each dose, creating a dose response curve (Figure 3.2.2), and the natural signal is then interpolated to find the equivalent palaeo-dose (D_e). Normalisation of the dose response curves is conducted by using a fixed test dose (T_x) administered at certain points throughout the whole protocol, accounting for any sensitivity changes in the individual aliquots. Information on the contributing dose rate (D_R) is also needed, and then the age of the sample can be calculated using equation 3.1:

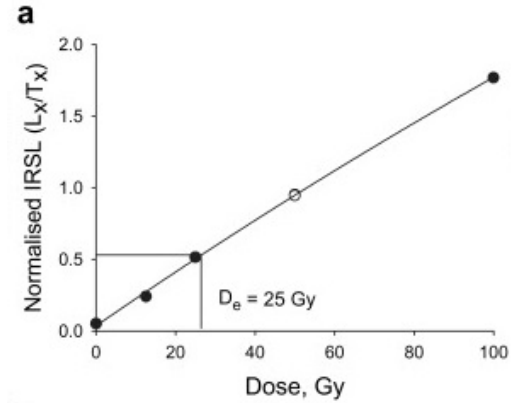


Figure 3.2.2. Example of a dose response curve and interpolated D_e . (Tsukamoto, et al., 2011)

$$Age (ka) = \frac{Palaeodose (D_e) (Gy)}{Dose Rate (D_R) (Gy/ka)} \quad Eq. 3.1$$

Infra-red stimulated (IRSL) and post infra-red stimulated luminescence (pIRIR) protocols are considered the most likely for achieving results, having been shown to be successful for stimulating a non-fading component by Tsukamoto et al (2011) using sedimentary feldspars. Other works also support the use of IRSL and pIRIR sequences, including Valla, et al. (2016), arguing that IRSL at 50°C (IRSL₅₀) was suitable for bedrock feldspars, producing consistent and reproducible results, but anomalous fading must still be accounted for. Several protocols have been developed to account for anomalous fading rates, producing g-values of % signal loss per decade, and have been applied to both sedimentary and volcanic feldspars. Research by Auclair, et al. (2003) presented 4 different tests for anomalous fading on coarse K-feldspars, varying stimulation times, location of pre-heat stages and delay periods. They successfully demonstrated that g-values were attainable from such material and that these measurements can be used for feldspar age correction.

The protocols used here followed a single aliquot regenerative (SAR) dose protocol allowing all measurements to be conducted on the same aliquot, with a correction to account for any sensitivity change. This method removes problems of individual grain or aliquot characteristics which may differ and increase scatter in the data. Two internal verification tests are incorporated; The recuperation test accounts for any signal which may be from e.g. thermal transfer which leads to anomalous signal behaviour. A zero-regenerative dose (L_0) is given, followed by the same T_x dose, and if there is

considerable deviation of the L_n/T_x ratio from unity, it indicates there is unwanted noise in the signal, most likely due to thermal transfer. The recycling ratio checks the adequacy of the sensitivity correction. The same L_x dose is given at the beginning and the end of every SAR cycle, and the ratio of the results is calculated. Measurements are typically discarded if values deviate >10-15% from unity (Tsukamoto, et al., 2014).

3.3 Applied methodology

The OSL core samples were stored and transported in light-proof containers, and prepared under laboratory darkroom conditions (dim orange light). The palaeo-dose (D_e) material was hand crushed in a pestle and mortar and then with a Retsch mm 2000 mixer mill. Dry sieving separated out grain size fractions of: <63, 63-90, 90-212 and >212 μm . Multiple rounds of settling the <63 μm fraction in water enabled the extraction of the <4 μm 4-11 and 11-63 μm size fractions.

All grain size fractions were subjected to preliminary TL, BLSL, IRSL and pIRIR sequences (Table 3.3.1) (Tsukamoto, et al., 2011), testing for quartz and feldspar components on 5 and 8mm aliquots. Two Risø OSL/TL readers, with $^{90}\text{Sr}/^{90}\text{Y}$ Beta sources, with a systematic error set at 2% and measurement errors set at 1.5% were used. Three different filters were used: A U-340 UV filter, an Interference I410 filter, then a Corning 7-59 and a Schott BG-39 filter pack to broaden the emission

Step	TL Sequence	BLSL Sequence	<i>IRSL50 & pIRIR Sequence</i>	Pulsed Double SAR	Observed
1	Dose	Dose	<i>Dose</i>	Dose	
2		TL at 220°C	<i>Pre-heat TL at 175°C</i>	TL at 220°C, 10 seconds	
3	TL at 450°C or 220°C	BLSL at 125°C	<i>IRSL at 50°C</i>	Pulsed IRSL at 50°C, 200 seconds	Lx
4			<i>pIRIR at 150°C</i>	Pulsed BLSL at 125°C, 200 seconds	Lx
5	Dose β 50 seconds	Dose β 50 seconds	<i>Dose β50 seconds</i>	Dose β 300 seconds	
6		Pre-heat 220°C	<i>Pre-heat 175°C</i>		
7	TL at 220°C	BLSL at 125°C	<i>IRSL50</i>		Tx
8			<i>pIRIR at 150°C</i>	Pulsed BLSL at 125°C, 200 seconds	Tx
9	BLSL at 230°C	BLSL at 230°C	<i>IRSL at 150°C</i>		Flush
10	Return to step 1	Return to step 1	<i>Return to step 1</i>		

Table 3.3.1 Summary of sequences run in this study, from Tsukamoto, et al., (2011)

detection window (320-480nm).

The IRSL₅₀ SAR protocol yielded the most promising results and became the focus for subsequent work. The pIRIR step was discarded due to a consistent lack of natural or regenerated signals (Figure 3.3.1). The preliminary tests produced dim signals from most samples, but the 4-11µm fractions from PI-07, PI-12 and PI-19 had shown the brightest luminescence, and were chosen to be the focus of subsequent IRSL₅₀ SAR tests for age determination. A standard feldspar anomalous fading test (Auclair, et al., 2003) was conducted on the 4-11µm fraction for these three samples irradiating the samples with 39 Gy, and stimulating with IRSL₅₀ after set time periods. Three g-values were calculated to account for any loss of signal which the samples suffered whilst in storage.

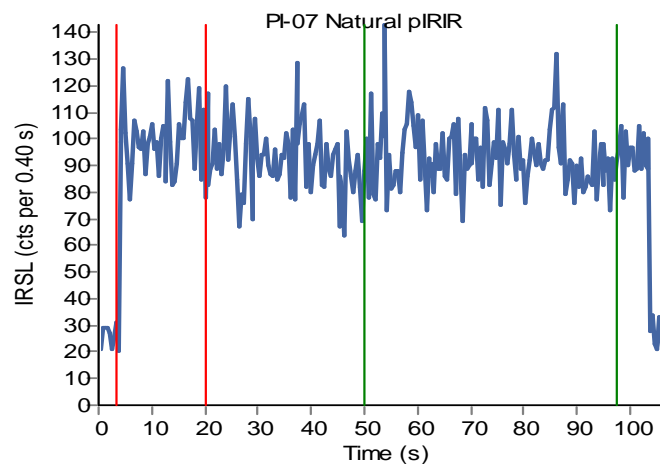


Figure 3.3.1 Example of a natural pIRIR signal from sample PI-07. No decay components are seen in any natural or regenerative signals, which were all dim and noisy.

Some of the 11-90 µm fraction for these 3 samples also underwent etching with 10% HF for a total of 40 minutes, washed twice in HCL (10% then 32%), then cleaned with demineralized water to remove some of the darker mafic components which were considered to be diluting the OSL signal. The etched fraction was subjected to a pulsed double SAR sequence (see Table 3.3.1). The luminescence signal was obtained using time-resolved OSL to isolate any quartz components, and detected with the U-340 filter. The 63-90µm fraction also became a focus point for test runs, undergoing three rounds of density separation with a 2.70g/cm³ heavy liquid, testing the lighter felsic fraction with IRSL₅₀ and pIRIR SAR sequences for age determination.

Four other Holocene age basalt also went through the same pre-processing stages to isolate the <4 µm to >212 µm grain size fractions. Each grain size fraction per sample was tested with the IRSL₅₀ and pIRIR SAR sequence. The 4-11 µm fraction was again focused on, and the samples were subjected to 1 further IRSL₅₀ SAR test for comparison with the Pico samples.

As a final test, all 10 Pico samples and the four 'other' basalt samples were subject to an IRSL₅₀ and pIRIR test, detected with a multi-band Hoya BG-39 short pass filter. The <63 µm fractions

were used for two 5 mm aliquots, as this grain size fraction was available for all Pico samples, and 1 aliquot each for the other basalts. The aim was to detect any emission signals which may be used for future exploration.

For each sample, the signal integration limits were standardised to maximise precision and signal used. The first 20 seconds of signal was taken as signal decay, and the last 50 seconds as the background integral. The recycling ratio limit was set at 15% from unity; following standards used by Tsukamoto, et al, (2014). Analysis of all of the data was conducted using the Risø Analyst software (Duller, 2015) and in Excel. Achieved D_e values which were >25% over the highest given dose within the SAR protocol were excluded from the age calculations as these were considered to be artefacts induced from high artificial doses on the sensitive samples.

3.4 Results

The results of the protocols from Tsukamoto, et al. (2011) were in summary, unsuccessful at producing distinct natural feldspar decay curves and D_e values with SAR protocols. The results of the preliminary BLSL tests for quartz were noisy, generally with <400 cps. The results of the TL tests were slightly more successful, stimulating a few TL peaks between 130-150°C, characteristic of quartz with some smaller peaks occasionally seen around 50°C showing shallow unstable traps emptying. Some samples also showed broad TL maxima at 250-300°C, more characteristic of feldspar emissions (Figure 3.4.1 A). Many aliquots showed slight count increases over the stimulation period, without peaks, most likely due to thermally induced transfer.

From the preliminary tests, samples PI-07 and PI-12 had provided notable TL signals (Figure 3.4.1 A and B). Sample PI-19 produced an IRSL₅₀ decay curve after undergoing the first round of density separation. From the 4-11µm fraction, a total of 90 aliquots were measured for sample PI-07, and 66 aliquots each for both PI-12 and PI-19. Each of the three samples did have at least some aliquots showing distinguishable natural decay curves, with examples shown in Figure 3.4.2, also with typical examples of D_e interpolation graphs and T_x/T_n results. From all the IRSL₅₀ runs only 20% of these aliquots produced SAR D_e values, with a high spread in D_e 's which were inconsistent within each test cycle, regardless of the sample.

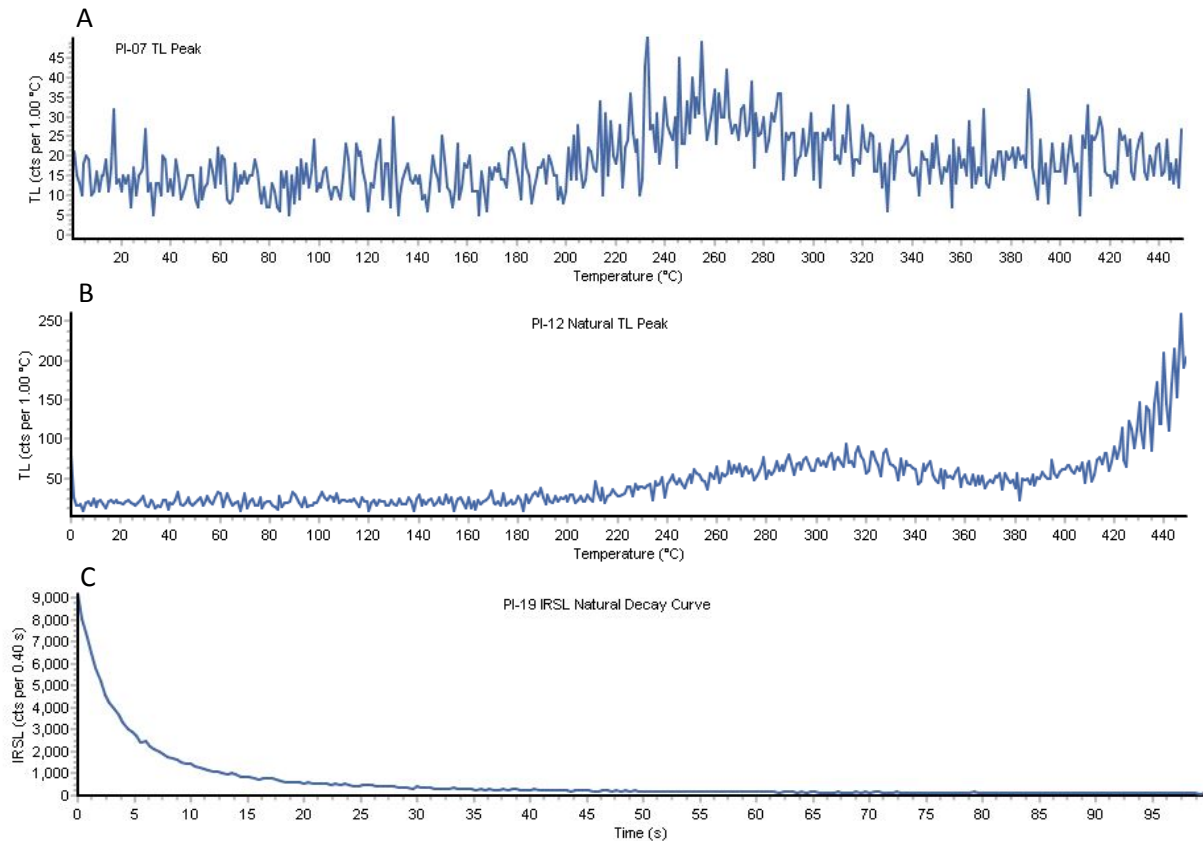


Figure 3.4.1 A: TL curve produced from PI-07, (50-90 μ m). No SAR stages were performed during this sequence. B: TL peak from PI-12, (63-90 μ m), small peak and noisy signal. C: Natural decay curve from PI-19 (63-90 μ m) after the first round of density separation.

Any D_e 's which were >25% from the highest given artificial dose were removed from the age calculation as this was seen as an artefact from irradiating the samples with high doses, leading to extrapolation of the equivalent dose (Top row in Figure 3.4.2). Only 14% of the achieved D_e 's were used for age calculation, with 5 D_e 's from PI-07, 15 from PI-12 and 11 from PI-19. Sudden changes in sensitivity are also seen from many of the aliquots with a drop in T_x/T_n after the first SAR cycle, indicating a high sensitivity to artificial doses which cannot be accounted for via the standard normalisation process, and can lead to positively skewed data and age overestimations in the unprocessed D_e 's.

With so few data points accepted statistical age modelling was not used (ideally $n=30$ are needed in standard dating applications (Cunningham, et al., 2011)) but the weighted mean and the median ages were calculated instead, as ways of statistically accounting for any spread in the small data set, using the measured natural dose rates, and the results are shown in Table 3.4.1.

The weighted mean and median ages for PI-07 both overestimate the radiocarbon age, but are both consistent with each other, supporting the possibility that the data set is reasonably precise. The two ages for PI-12 are also very similar indicating that despite the small sample number, with the ages matching the ^{14}C age within errors, there is good accuracy and precision in the data. The weighted

Sample	Expected		Weighted Mean		Weighted		Median		Median	Mean
	Age (ka)	N	De (Gy)	Error	mean Age (ka)	Error	De (Gy)	Error	Age (ka)	AbsDev
PI-07	0.3	5	5.93	1.66	2.78	0.79	5.61	0.85	2.64	0.41
PI-12	1.65	14	2.57	1.20	1.24	0.58	3.22	1.01	1.55	0.49
PI-19	3.86	10	1.55	1.44	0.88	0.82	5.38	2.08	3.05	1.19

Table 3.4.1 Weighted mean and median De's (Gy) and respective ages.

mean age for PI-19 is several orders lower than the expected ^{14}C age, with a much smaller weighted mean than median indicating there is still some spread in the D_e data leading to a skewed weighted mean age, but the median age with error corresponds to the expected age. The Median ages are accepted here as the most reliable ages as it is a stable statistic for small data sets which show a spread in values.

The results of the fading test (end figures in Figure 3.4.5) were also poor with only one sample producing a g-value with an error <10%. For sample PI-12, a g-value of $3.84 \pm 2.55\%$ was obtained, but the other two samples produced significantly higher g-values of $13.96 \pm 13.25\%$ for PI-07 and $15.39 \pm 17.37\%$ for PI-19, which were rejected for use due to such high errors.

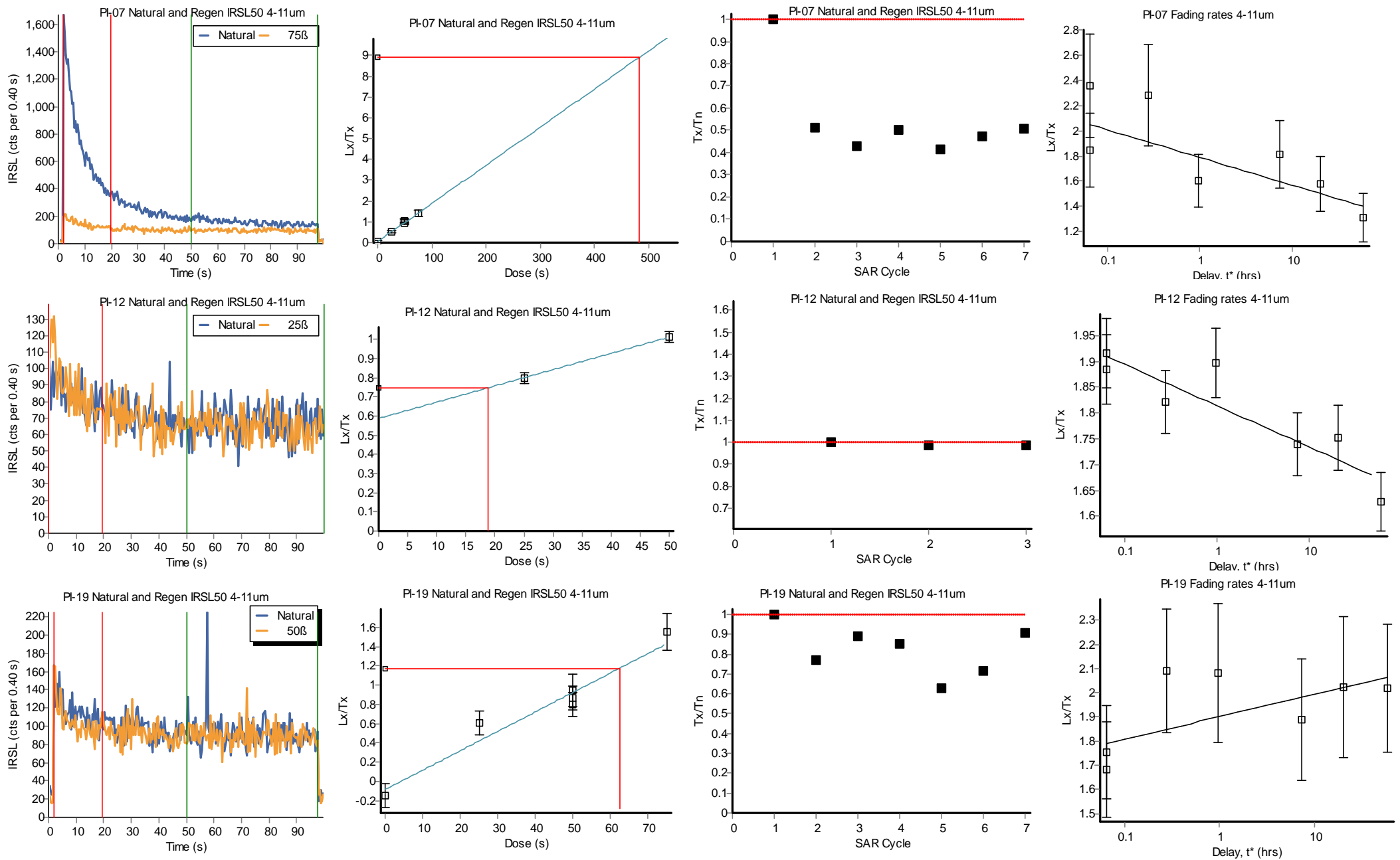


Figure 3.4.2 Examples of natural and regenerated decay curves, dose response curves and Tx/Tn plots to show sensitivity. An example Lx/Tx graph from the fading test is also included for each sample on the far right. Top row shows PI-07 examples of a high extrapolated De value in response to high laboratory doses, which is also seen in the drop in sensitivity with the first SAR cycle, and response to lab doses.

The pulsed double SAR protocol used on the HF etched 11-90 μm fraction yielded discouraging results with very low natural photon counts from both the natural IRSL and BLSL stages. The time-resolved BLSL signals showed a very rapid decline in counts between the on and off times (Figure 3.4.3) and a lack of a clear decay component, which may be indicative of unsensitised quartz within the basalt which is not suitable for dating (Guralnik, et al., 2015), but the presence of quartz does fit with the observation of some TL quartz peaks between from the preliminary tests. Irradiating the samples with a high dose of 41.5 Gy significantly increased the counts with regenerated decay curves detected, but since this artificial dose is significantly larger than the natural dose, and the produced curves were dissimilar to the natural signals the pulsed double SAR protocol was not experimented with further.

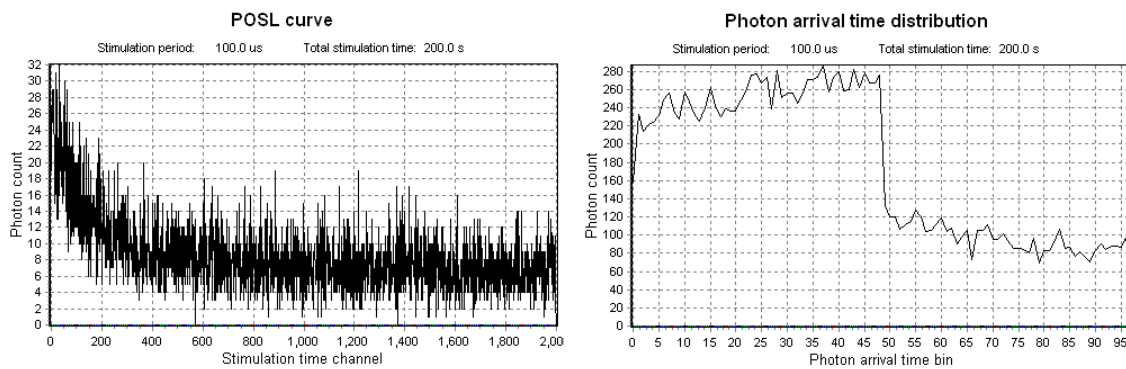


Figure 3.4.3. Left: Natural Pulsed BLSL decay curve from sample PI-12, showing a small and noisy emission obtained over the whole pulsed stimulation period. Right: Distribution of photon arrival times between gating times for the natural pulsed BLSL step. No clear quartz or feldspar decay component is seen; with the sharp decrease in photon counts around bin 45-50 possibly a product of the switching off of the stimulation, or may indicate the presence of unsensitised quartz (Guralnik, et al., 2015).

The 63-90 μm fraction underwent 3 rounds of density separation and IRSL₅₀ testing. A total of 21 aliquots for PI-07, 29 aliquots for PI-12 and 35 aliquots for sample PI-19 were tested. From these tests, sample PI-07 produced one D_e value, PI-12 produced 4, and PI-19 produced 5. The best results were achieved after the third density separation which produced strong natural and regenerated decay curves with high counts, but the sensitivity of all the samples was still very high, with unpredictable T_x/T_n ratios after each SAR cycle. All D_e 's were >25% from the highest given dose and with the small number of D_e values recovered ages were not calculated.

Applying the same IRSL₅₀ and pIRIR sequences to the four other basalt samples for dating was unsuccessful. All grain size fractions per sample produced noise-dominated emissions, with only D_e values being produced from HW-10 (2.02 ± 1.26 Gy) and TF-6 (2.93 ± 1.81 Gy). The samples all showed high sensitivity to regenerative doses, with no systematic pattern to the test dose response, and were not tested further. The results of the final IRSL and pIRIR test sequence, with all 14 samples' emissions detected with a short pass Hoya BG-39 filter produced high counts and no recognisable

natural signals from any sample. All natural and regenerated signals increased to ~1500 counts where the signal plateaued. The sensitivities were all relatively low, with little deviation between the Tx and Tn emissions. This is probably due to such high counts being registered through the filter, any characteristics of the sample are not discernible anyway, and thus the lack of changing sensitivity seen here is redundant. The results are generally inconclusive from this test with no useable luminescence signals from any measured sample.

3.5 Discussion

Using IRSL₅₀ on these Holocene volcanic feldspars was suitable for producing D_e values for calculating ages for three samples. The IRSL₅₀ median age from sample PI-07 vastly overestimates the ¹⁴C age but the ages for PI-12 at 1.55 ka and PI-19 at 3.05 ka correspond to their independent ages, despite the low success rate of 14% of all IRSL₅₀ measured aliquots used for age calculation.

Several possible explanations can be presented as to why the results from these tests were so variable between samples and between aliquots. Too few data was collected to be able to fully address any possible effects of using two different Risø readers for the measurements, and thus any possible systematic differences between the obtained results are ignored. The U-340 UV filter was only suitable for detecting quartz components- which were scarce here - and using the I410 interference filter was also inadequate as the number of counts from the feldspar emission centres was just too low to be detected. This can explain the poor preliminary TL and BLSL results as any feldspar emissions from all 10 samples may have been missed or just too dim to detect. The combined Corning 7-59 and Schott BG39 (320-480nm) filter pack was suitable for widening the detection waveband and using alongside the subsequent IRSL₅₀ tests. The use of the wrong filter may explain the results of the pulsed double SAR run, where no discernible feldspar emissions were characterised as the UV filter may have been missing the tail of the feldspar peak. Another explanation could be due to the treatment with the 10% HF which may have etched away too much at the felsic components and thus given no/little suitable material to be tested.

The lack of results from the 7 Pico samples which were not explored past the preliminary TL, BLSL and IRSL tests can be explained alongside the mineralogy. Whilst all samples were compositionally similar, with plagioclase rich groundmasses, there were samples which lacked a plagioclase phenocryst phase. The three samples which were used for age determination all had ≤65% estimated plagioclase phenocrysts which are arguably the primary emission centres. However, with further processing of the other 7 samples by density separation and using the right filter it is possible that ages may be achieved from the rest of the samples, utilising the smaller feldspars from the groundmasses.

This fine-grained groundmass can explain the success of using the 4-11 μ m fraction for IRSL₅₀ dating. These plagioclases were all <500 μ m in length, constituting an estimated 42% of the groundmasses. During the crushing and dry sieving preparations, the minerals may have been liberated from other minerals and, assisted by any present plagioclase phenocrysts, light stimulation and emission detection was most likely made easier. The variation in D_e's produced using this size fraction are likely a product of the rapid crystallisation of the groundmass, producing disordered crystals which struggle to build up a stable signal, as well as in-sample chemical variations which have different trap depths and stabilities. This can explain the variable and fewest results achieved from PI-07 which presented the highest ranges in K and Na content, leading to different emissions with different stabilities between feldspar crystals. This can be seen in the change in L_x/T_x with many of the aliquots, often showing a decrease in sensitivity with each SAR cycle or unpredictable behaviour in response to the subsequent test doses (Tx). PI-19 did not have much compositional variation, with all low-K and Na contents, but as this sample is oldest, the feldspar crystals are possibly to be more ordered than in the younger samples as the crystals slowly configure their internal structures to reduce the total energy, leading to more distal electron-trap recombination paths and the build-up of luminescence signal suitable for age determination.

The calcium-rich composition of the samples is also likely to negatively influence results, with fading rates found to increase with increasing Ca contents (Panzeri, et al., (2012); Valla, et al., (2016); Huntley, et al., (2007)), and with all feldspars which were measured with the EDS having >50% An, this high Ca content may lead to few distal electron-trap recombination pathways which contribute to the stable signal components (Reimann, et al., 2015). This can also explain the lack of success with using the post-IRSL stage, which has been previously found to stimulate a non-fading component (Li, et al., 2014), but here with the high Ca, there may lack a non-fading pIRIR component altogether.

The results of the fading test were poor but, as the samples were irradiated with a much higher dose (39 Gy) than what would have naturally occurred for the young basalts, the obtained g-values were not accounted for during the age calculation, as they were considered unrepresentative for the young samples which were producing unpredictable and noisy results. With the high Ca contents, it is considered that if these samples were older with stronger luminescence signals, the fading rate would most likely be high and would be more easily measured.

Calculating the ages with the median values was seen as the best option for the very small data set which was collected, as the spread of the data could be accounted for without deviating towards outliers. Calculating a weighted mean age with such dim signals was deemed less appropriate as it is hard to weight the results appropriately with all signals being dim and hard to differentiate. Discarding D_e values >25% from the highest given dose within the SAR cycles removed very high D_e values which were most likely artefacts from irradiating the samples with a high dose which would lead to

high extrapolated D_e 's, which are not representative of the natural palaeodose and leading to age overestimations. Ideally there is a need for more aliquots to bulk up the data set and increase accuracy and precision in the age calculation.

The success of the 63-90 μm results after the three rounds of density separation at producing natural and regenerated decay curves poses as the most promising stage to include as part of basalt sample preparation. It is clear that the high proportion of mafic minerals was diluting the luminescence emissions, and the density separation isolates the feldspars which are less likely to be completely disintegrated in this grain size fraction compared to the 4-11 μm . However, as many of these samples have been found to be very sensitive to regenerative doses, density separation may not lead to dating success, with continuing difficulty developing dose response curves and achieving D_e values. The results from the other four basalts were noisy and unusable, and this could be due to extended storage time or light exposure. The samples were not intended for OSL measurements and thus appropriate light-proof sample collection and storage procedures were not followed, exposing the cores to extensive light which may have decreased the number of trapped electrons. The mineralogy of these samples was not addressed here, and from literature it was believed the feldspars would be plagioclases with various An%, which will have definitely influenced the samples' abilities for signal growth and led to variable results.

In conclusion, the characterisation of the luminescence signals was difficult, with small and noisy natural and regenerated signals which vary in shape and length. The mineralogy holds a strong answer as to why the results were so poor, with the high Ca leading to high fading rates and low internal potassium influencing the dose rates. These samples may also just be simply too young to have significant natural signal build up in stable traps with these low dose rates, requiring more time for any further crystal growth and ordering and for stable traps to be filled. With regenerated signals successfully attained, it is clear there is some potential for utilisable signal accumulation, indicating that Ca-rich feldspars of older ages have future potential for luminescence dating. The reproducibility of these tests is poor, but with the successful acquisition of three ages using statistical quality control, it would be advisable to apply these methods and protocols to other dated Holocene-age basalts of different mineralogy, with independent ages and known sampling techniques.

4. Palaeo-Magnetic Intensity

4.1 Introduction

With the Earth's Magnetic Field (EMF) as a vector quantity having both direction and magnitude, it is possible to identify past changes in magnetic characteristics, captured by magnetic minerals in the geological record. As any three-dimensional property, the EMF can be quantified with the three scalars: inclination, declination and intensity (Figure 4.1.1). The magnetic inclination (I°) is defined as the angle between the horizontal plane and the magnetic field lines. Magnetic declination (D°) is defined as the angular difference on the horizontal between the geographic North and the magnetic north. Together D and I describe the direction of the magnetic field, which changes over geological time, with polar wanderings documented for the past 200 Ma (Schettino & Scotese, 2005).

The third parameter is the magnetic intensity (B , μT), which refers to the strength of the magnetic field, determined by the density of magnetic flux lines. The magnetic intensity is the focus of this study, and today the field strength ranges between $25\text{-}65\mu\text{T}$ (Tauxe, et al., 2014)

The EMF arises from the 'geo-dynamo', produced by magneto-hydrodynamic liquids in the Earth's outer core. This dynamic origin explains why the EMF has varied at different spatial and temporal timescales. It has been noted that the moment of the

magnetic dipole has been decreasing, by $\sim 8\%$ over the past 150 years and could be indicative of an upcoming dipole reversal (Jackson, et al., 2000). The local field can rapidly change with intensity fluctuations of at least $20\mu\text{T}$ per century seen around Europe (Gomez-Paccard, et al., 2012). The South Atlantic Magnetic Anomaly (SAMA) is an area with a low total magnetic intensity and deviating directions (Figure 1.2.1), which lies over the southern half of the Atlantic Ocean and Eastern South America. The history of the anomaly has been addressed and has been found to show an increase in area and a westward and southward drift since the 1600's (Hartmann & Pacca, 2009).

The island of Pico lies north of the equator, but the SAMA is believed to have an expression on the behaviour of the EMF at this location. With a geologically recent and dated eruptive history, the volcanic products present an ideal study location to characterise the movement and changes of the SAMA phenomenon.

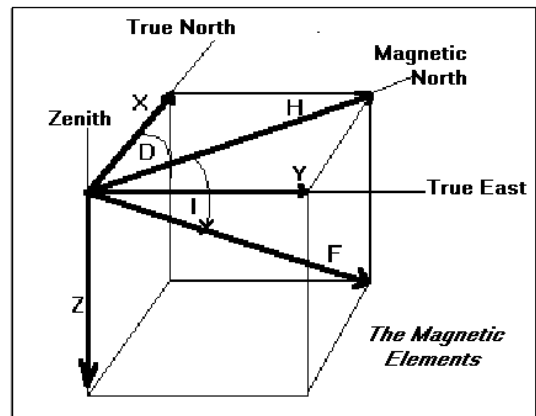


Figure 4.1.1 Magnetic Vectors. X: North component, Y: east component, Z: vertical intensity, D: declination, F: total intensity, H: horizontal intensity and, I: Inclination. (NGDC, 2016)

Conventional methods for measuring PMI's- such as those based on the ideas of Thellier & Thellier, (1959) calculate an absolute PMI value first by comparing a samples' natural remnant magnetism (NRM) to a laboratory induced normaliser, such as a thermo-remnant magnetisation (TRM). This conventional method uses a pre-heating stage and different heating stages during measurement, which are known to potentially induce adverse alterations in the magnetic characteristics of the minerals, leading to a decrease in initial susceptibility and induced magnetisation (Collinson, 2013). The Pseudo-Thellier method (pTh) has been developing over the past few decades and avoids this, using instead an Anhyseresis Remnenat magnetisation (ARM) normaliser for the NRM to calculate a relative PMI value, which is then calibrated to an absolute PMI value. Initial studies applied the pTh method to marine cores, already from the Azores region, creating a chronology of PMI changes over the past 276 ka (Kruiver, et al., 1999). They found similar results to the conventional records, providing promise for the methods' future applications and development and further use of this method on basalts which was first performed by De Groot, et al, (2013).

The pseudo-Thellier method was applied to 21 Holocene-age samples from the island of Pico (see Table 1.1) to determine the palaeo-intensity history over the past 3 ka years. The pseudo-Thellier 2G DC-SQUID magnetometer (A.K.A the 'Robot') at Fort Hoofddijk at Utrecht University was used for the measurements. The four other basalts from the islands of Hawaii, Tenerife, Gran Canaria and Terceira were not measured with the pTh method as they had already been tested for PMI values using multi-method approaches, and will not be discussed further.

4.2 Theoretical Background

Sedimentary and volcanic rocks contain a multitude of ferromagnetic minerals which can record and retain a magnetic vector. Magnetic properties arise as a result of the electron spin directions coordinating into low total energy configurations, as they cool towards their curie temperatures (T_C). During cooling, external energy such as that from the EMF inflicts its signature characteristics on to the minerals, altering the electron configuration which is captured (Tauxe, et al., 2016/17). This stored primary magnetism is termed the natural remnant magnetism (NRM) and remains from the time of formation once the external field is removed, until it is altered by a later thermal or magnetic event. The NRM captured depends on the geomagnetic field, rock forming processes and rock history, and is usually composed of more than one component (Butler, 1998). If a sample has been subjected to chemical, thermal or physical alterations, a secondary NRM signature may be over-printed which must be recognised and accounted for.

The pseudo-Thellier approach (pTh) was developed in the 1990's, initially applied for relative PMI determination on carbonate-rich sediments, removing risks of viscous remanence in the minerals (Tauxe, et al., 1995). The technique compares a samples' NRM to an acquired Anhyseric Remnant

Magnetisation (ARM), acquired through exposure to a high alternating field (AF) and a smaller DC field, producing a relative PMI (Equation 4.1). The method has been recently addressed for its use for determining absolute PMI values, and its comparability to conventional normalisers such as thermoremanent magnetisation (TRM) (Yu, et al., 2003). Application of the pTh approach on to volcanic deposits was first conducted by De Groot, et al. (2013), using basalt samples from Hawaii and a multi-method PMI approach, the samples were measured for relative PMI values. The results were calibrated by plotting a linear fit through the accepted pTh slopes on the reference geomagnetic field which produced a calibration curve (Figure 4.2.1) and derived equation 4.2 used to calculate absolute PMI values.

$$B_{\text{palaeo}} = \frac{\text{NRM}}{\text{ARM}} \times \text{Artificial field intensity} \quad \text{Eq. 4.1}$$

$$B_{\text{abs}} = 7.718 \times \text{pTh slope} + 14.600 \quad \text{Eq. 4.2}$$

At Utrecht university, the 2G- DC SQUID magnetometer (A.K.A. the ‘Robot’) was used for measurements, where samples undergo 3 (de-) magnetising stages to acquire the NRM and ARM values used to calculate the relative PMI value. First, the NRM is acquired and removed by comparing the natural magnetic moments to an applied AF of increasing strength (Butler, (1998); Tauxe, et al., (1995)), demagnetising along 3 orthogonal axes (x, y, z).

Next is the ARM acquisition, where the AF strength is increased in the same step-sizes, inducing increased magnetisation, followed by a static DC field of 40 μT , magnetising the central axis in one direction. The final stage is a step-wise demagnetisation of the ARM. The NRM remaining over ARM acquisition is plotted in an Arai-style plot, and the best-fit pTh slope (m) is calculated with at least 4 points and used in Equation 4.1 to gain the relative PMI value.

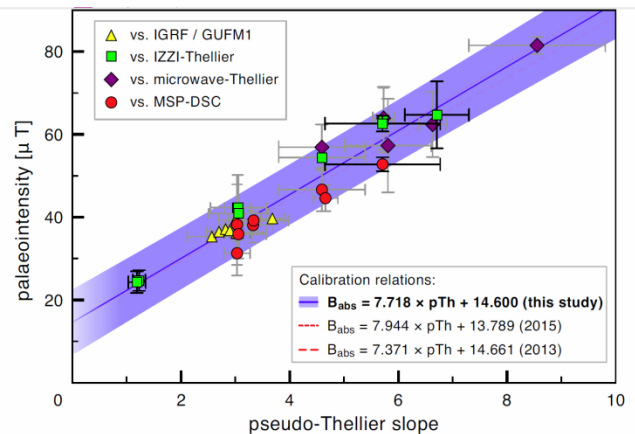


Figure 4.2.1 Calibration curve and equation used for relative to absolute PMI calibration. (de Groot, et al., 2016)

A strict statistical control is applied, first selecting the samples with suitable grain size ranges. This is done by calculating $B_{1/2ARM}$ values which indicate the AF strength which imparts half of the saturated ARM in a sample, and is indicative of grain size. Large $B_{1/2ARM}$ values represent smaller grains with higher saturation and coercivities, favourable for PMI determination (Yu, et al., 2003). For samples with a $B_{1/2ARM}$ between 23 and 63 mT, the pTh slope is shown to linearly depend on the geomagnetic field which the sample formed in; the ratio of the pTh slope to the reference geomagnetic field intensity should be unity (De Groot, et al., 2013) (Figure 4.2.2).

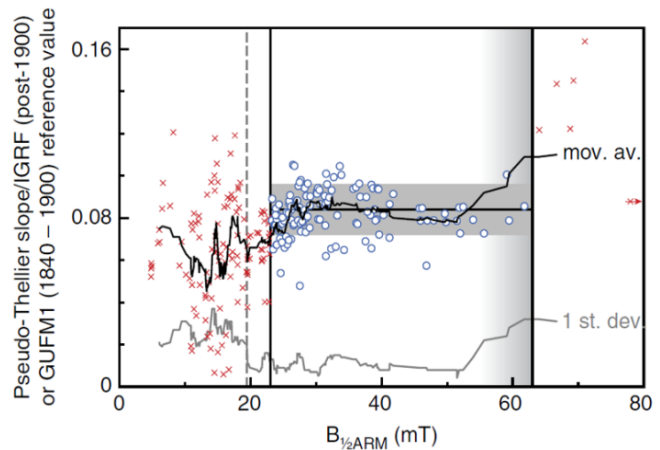


Figure 4.2.2 pTh results normalised with the Global Geomagnetic reference field over $B_{1/2}$ ARM values. Between 23 and 63 mT, there is a linear and stable relationship between the pTh results and $B_{1/2}$ ARM values. (De Groot, et al., 2013), and these limits are used to separate accepted and rejected pTh PMI values.

The results from the NRM demagnetisation can be used to plot D and I directional data. This data can indicate whether the sample experienced magnetic overprinting, leading to a secondary NRM either before or during the NRM demagnetisation, which would not reflect the primary imparting field. It can also indicate in-unit consistency of the samples; If 1-2 samples produce significantly different directions it could indicate sampling of two different units.

Zijderveld diagrams are used to display directional data, producing a plot of the vector magnetisation during AF demagnetisation on to 2 orthogonal planes, representing the horizontal (H vector) and vertical (Z vector) projections (Figure 4.2.3 A) (Dunlop, 1979). These slopes, if linear show the primary NRM, but if more components are present towards the origin, they may indicate a secondary NRM. The distance between the points and the origin is proportional to the NRM intensity (Butler, 1998). To calculate the mean direction, a best fit slope is defined selecting at least 4 points on the vector to interpolate (open and closed points, Figure 4.2.3 A), and the mean palaeo-direction is determined with these.

Equal Area Projection plots are also used for directional data (Figure 4.2.3 B) displaying both the inclination from the vertical axis and declination from the outer circle. This plot indicates whether there has been alteration of the magnetic moments along either of the vectors. If there has been no change in the NRM, i.e. if all points have the same direction, all the points on the plot will lie in the same location.

Mean D and I values are determined, as well as a measure of data dispersion (k). This parameter is 0 if the directions are randomly distributed, and infinity if all directions lie on the same

point, and here values are accepted if k lies between 50 -1000. Alpha 95 confidence intervals were also calculated, as a statistical measure of accuracy and precision, with values rejected if outside of 2 standard errors from the mean (Butler, 1998).

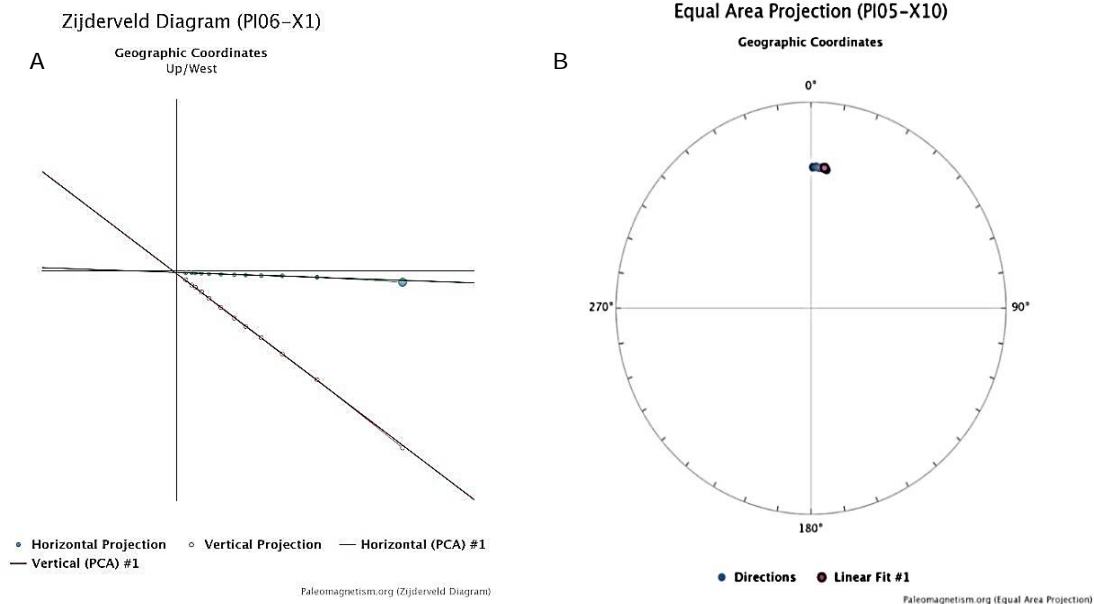


Figure 4.2.3 A) Example of Zijderveld diagram, with linear vectors and no directional changes or secondary NRM observed. The inclination is not determinable from this graph B) Example of an equal-area projection plot where there is a very small wander of the vectors. The declination can be read from the outer circle, and the inclination from the vertical axis. Both plots are from paleomagnetism.org.

4.3 Applied Methodology

Six cores from 21 locations were chosen and 6-8mm thick slices were cut from the ends of the cores using a water-cooled precision saw. These samples were then aligned cemented into plastic cubes with silicon cement, and loaded into the 2G DC-SQUID magnetometer.

To measure and demagnetise the NRM, the samples were subjected to 12 AF field steps from 0 mT to 100 mT (Figure 4.3.1), then manually demagnetised in an AF of 300 mT, as the robot is not capable of reaching fields higher than 100 mT. The ARM was then acquired again, with a manual subjection to an AF of 300 mT as well as a DC field at 40 mT., before the samples were demagnetised again in the same steps.

The results were processed with a Macro in Excel developed by A. Béguin at Utrecht University. The arai-style plots were made, and a line of best fit was calculated, with uncertainties at 1σ . The $B_{1/2ARM}$ criteria was assessed and the samples which passed were grouped by age (to within the same decade), and average PMI values were calculated per age group, unless only one sample was available.

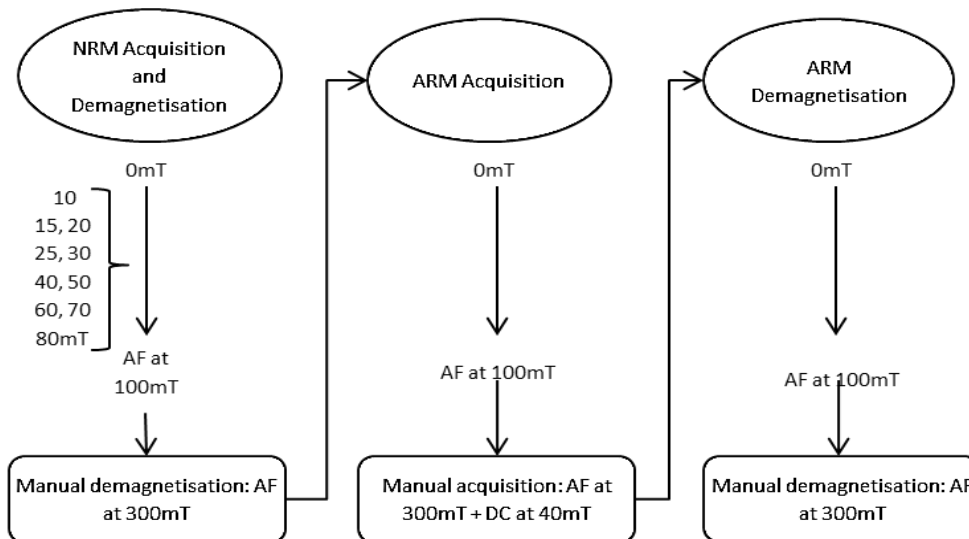


Figure 4.3.1 Flow chart of stages for pTh measurement, with values of step-wise field application.

The NRM demagnetisation data was then used to plot the directional data where Zijderveld diagrams and equal area projection plots were presented and the data sets were checked for any signs of over printing or magnetic moment alterations during the NRM demagnetisation. This was performed using a program available at: <http://paleomagnetism.org/> (Koymans, et al., 2016).

The final PMI and directional results were combined with the results from the IZZI-Thellier and the microwave-Thellier PMI tests which were conducted by BSc students at Utrecht University (Wassing, (2016); Gülcher, (2016) and Van Grinsven, (2016)), as well as three geomagnetic reference models (PFM9K.1b, SHA.DIF.14K and the IGRF12) and results from neighbouring islands.

4.4 Results

A full range in unprocessed palaeo-intensity values were obtained, falling between 25.5 μT and 127.8 μT . Between the 6 individual samples per site location, there was some spread in results, with 10-20 μT differences often seen between some of the samples per location. PI-10 had the largest range of PMI values from its 6 samples, with an average of $70.8 \pm 28.7 \mu\text{T}$, and PI-13 had the lowest range, with an average of $22.6 \mu\text{T} \pm 1 \mu\text{T}$.

Addressing the Arai-style plots most samples had good linear relationships between the NRM remaining and ARM gained. Only ~5-6 samples showed any slight changing behaviour, with 1-2 points changing direction within the first couple of demagnetisation stages, but these were seen as demagnetisation of unstable vector components and discounted from the pTh slope calculation. The AF ranges for the pTh slope were usually between 10-25mT and 15-30mT, and all R^2 values were ≥ 0.967 (PI19-X7). Figure 4.4.1 presents examples of Arai-style plots from three samples which show generally linear relationships, apart from PI-19 where strange linear behaviour is seen with the sample not being magnetised until around 1.0 mAm^2/kg .

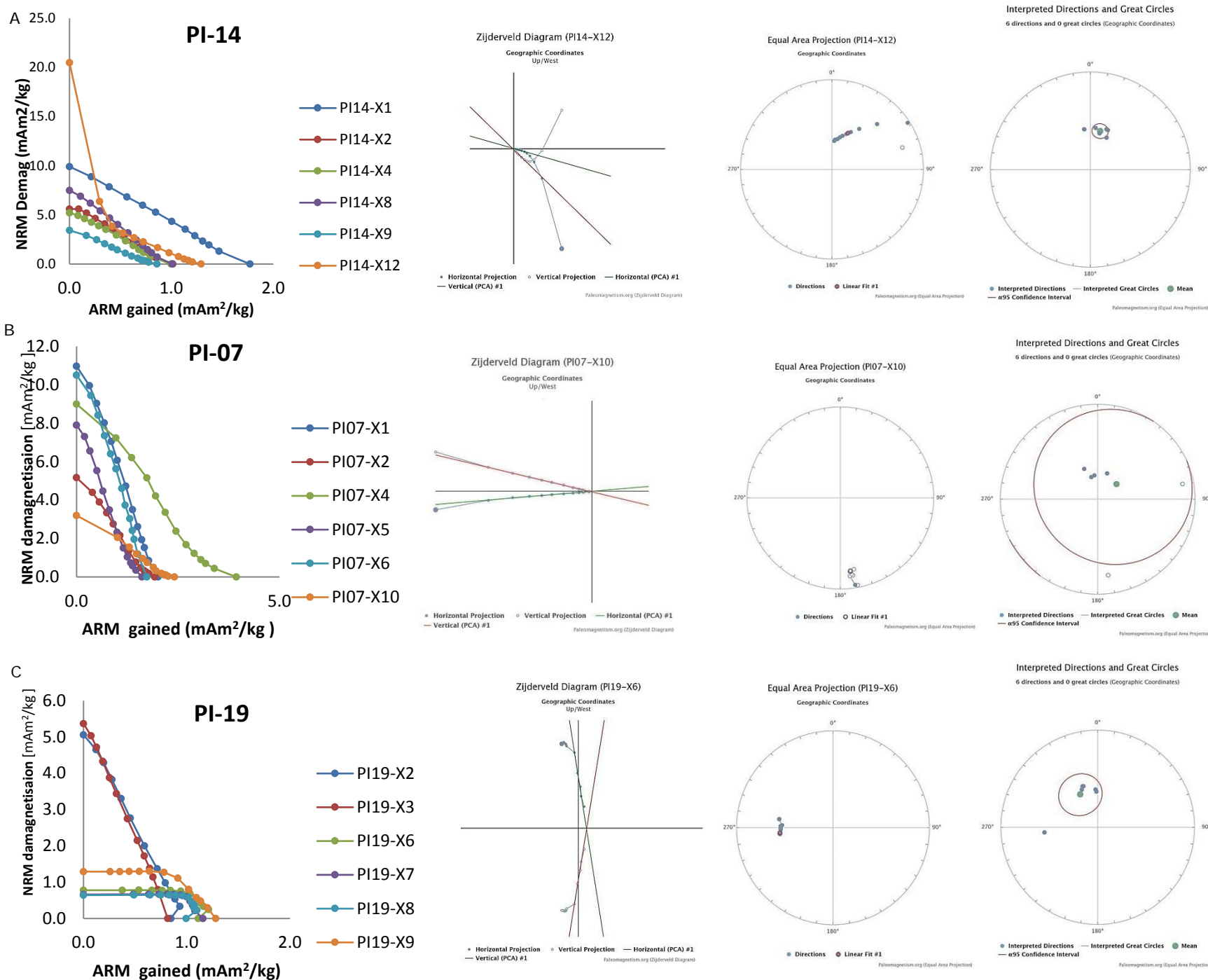


Figure 4.4.1 Example arai-style plots from PI-14, -07 and -19 and corresponding Zijdeveld diagrams, equal area projection (EAP) plots and summary directional circles. PI-14 shows a strong change in magnetisation after the first 2 steps, and some directional wander in the EAP. PI-19 shows differences in NRM demagnetisation over ARM gained, with one sample showing anomalous directional behaviour.

Accepted/rejected PMI results

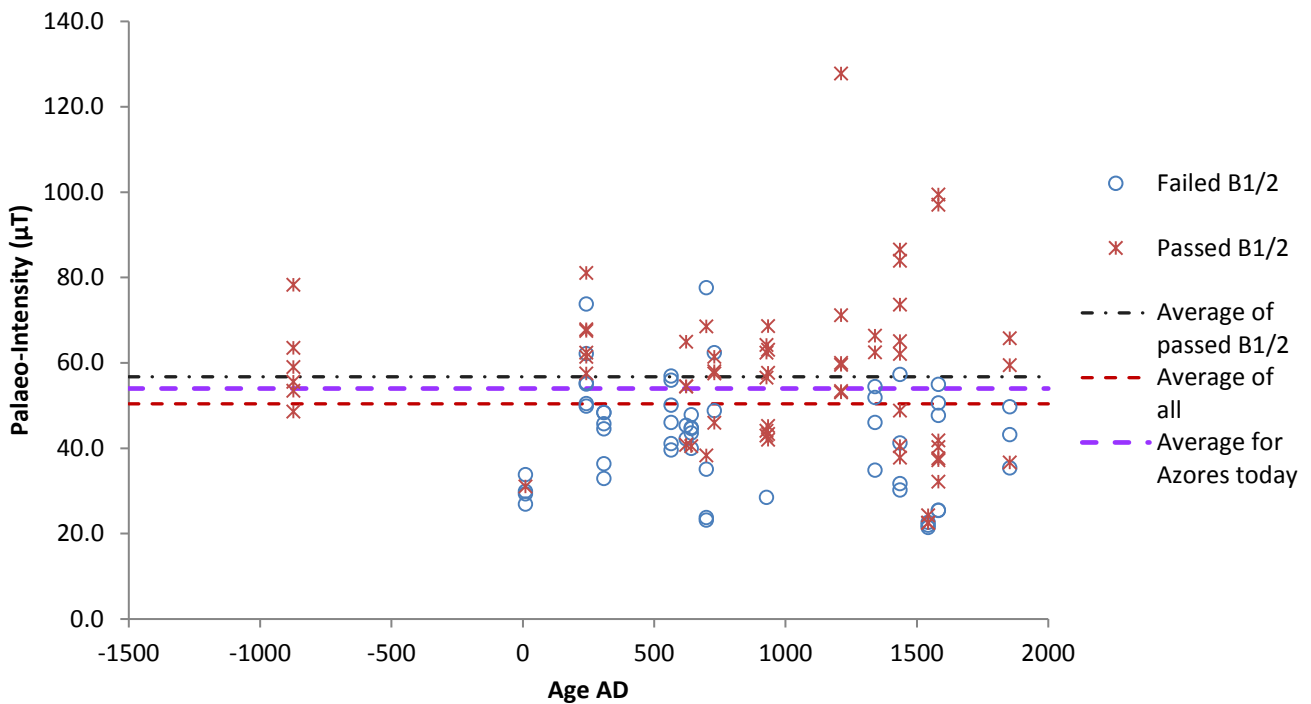


Figure 4.4.2 Range of PMI (μT) values produced from all samples, and display of whether these values passed or failed the first statistical criteria, and comparison with the expected field.

Sample ID	Age (AD)	Count	Individual PMI's (μT)	Average PMI (μT)	σ	β
PI-14	-873	6	59.0, 48.6, 63.5, 55.6, 78.3, 53.4	59.7	10.4	17%
PI-13	1543	3	22.5, 24.3, 22.6	23.1	1.05	5%
PI-05	1346	2	62.5, 66.4	64.4	2.76	4%
PI-11	719	4	58.1, 57.6, 45.9, 61.5	55.8	6.76	12%
PI-15	630	4	65.0, 40.8, 54.5, 54.5	53.7	9.91	18%
PI-07	1720	5	56.5, 43.0, 44.1, 64.2, 62.4	54.1	10.01	19%
PI-17/18	247	6	62.4, 61.4, 67.5, 57.5, 67.9, 81.1	66.3	8.23	12%
PI-03/04	1719	5	97.1, 99.5, 40.3, 41.9 37.2, 32.2, 37.7	37.8	3.7	10%

Table 4.4.1 Summary results from the Pseudo-Thellier PMI tests for the Pico samples. Individual sample PMI values are shown, along with the final averaged PMI value per age group, standard deviation and beta (sigma/average) values.

Of the 126 samples, 50.8% passed the $B_{1/2ARM}$ criteria, with a maximum $B_{1/2ARM}$ of 51.4mT - well within the maximum limit of 64mT. Figure 4.4.2 shows the range of obtained PMI values (μT) per age group (AD) and whether they passed or failed the $B_{1/2ARM}$ criteria. Samples PI-06, -21 and PI-22 had all 6 samples fail this $B_{1/2ARM}$ criteria, and not analysed further. The current total intensity for the Azores is also plotted at 43.74 μT (IGRF, 2014) (dashed purple line), and it is observable that the average of the passed results provides a higher PMI value than the average PMI today. Two values from PI-03 were also discarded from the final PMI calculation for PI-03/04 as they were anonymously high ($\geq 97 \mu\text{T}$) leading to an average PMI of $55.1 \pm 29.7 \mu\text{T}$, compared to the accepted final value of $37.8 \pm 3.7 \mu\text{T}$. Eight PMI values out of the total 13 age groups were accepted, having β values $\leq 20\%$. The final processed PMI values were found to be close to today's average intensity of 43.74 μT around the Azores. PI-13 presented the lowest value at 23.1 μT , followed by PI-04 at 37.2 μT . The rest of the samples (PI-05, -11, -15, -07, -17/18 and -14) produced values ranging between 53.7 and 66.3 μT . Table 4.4.1 presents the full results.

Five results from the IZZI-Thellier and 2 results from the Microwave-Thellier PMI tests (Van Grinsven, (2016) and Gülcher (2016)) were plotted against the corresponding pTh results (Figure 4.4.3). There is a good relation between the two data sets, with overlapping confidence bands and a clustering of the points around the 1:1 line, with one outlier from the Microwave-Thellier measurements which had an anomalously high PMI of 100.45 μT .

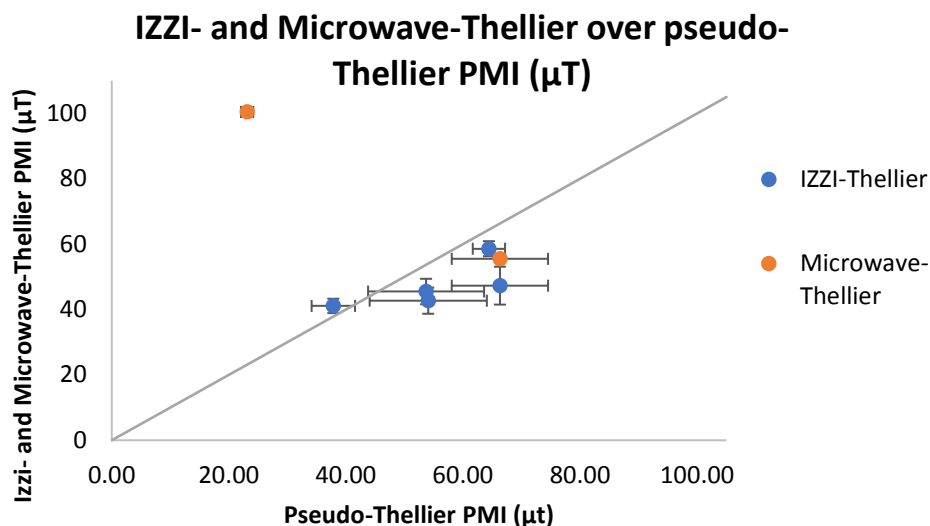


Figure 4.4.3 Comparison of the IZZI- and Microwave-Thellier results with the Pseudo-Thellier results obtained here. Vertical and horizontal error bars represent PMI sigma values.

Finally, the obtained palaeo-intensity values were plotted over the ^{14}C dates (Figure 4.4.4), which were calibrated using intcal13.14C radiocarbon calibration curve. The reference geomagnetic intensity models IGRF.12, PFM9K.1b and SHA.DIF underlie the results. The vertical errors in show PMI sigma errors and the horizontal bars show standard 1 probability intervals from the Intcal13.14C calibration. Data from surrounding islands of Terceira (de Groot et al. 2016), and Sao Miguel (di Chiara et al. 2014) as well as the PMI values from the IZZI- and Microwave Thellier experiments conducted on the Pico samples (van Grinsven, BSc thesis, 2016; Gülcher, BSc thesis, 2016) are also plotted to compliment the results obtained here.

Four of the pTh points lie within the 1σ confidence interval band for the PFM9K.1B model, but the rest of the points do lie outside of this. Values at 1346 and 1400 AD are higher than the decreasing field intensity shown in all the models, but the large 1σ errors (vertical error bars) do fall within ranges of the other PMI values from the IZZI-Thellier results from Pico.. The pTh results are also consistent with the results from the neighbouring island of São Miguel, which also show some spread, but have overlapping errors with the pTh and the reference models.

Directional Data

After addressing the palaeo-directions, it was clear that most of the results showed little evidence of altered NRMs, with mostly a linear demagnetisation towards the origin, indicating that the attained pTh values are representative of the primary and not secondary NRM. From the Zijdeveld plots Samples PI01-X9, PI02-X1, PI12, PI13 and PI14, show slight changes in magnetisation after the first demagnetisation step of 10mT (e.g. Figure 4.4.4) indicating removal of low-stability components (Butler, 1998) and not of secondary NRM.

Sample PI14-X12 shows the strangest behaviour (Figure 4.4.5), with a clear directional change between stages of 20 and 25mT. Sample PI19-X6 presented directional data which orientates 90° from the majority of the rest of the samples (Figure 4.4.3 C), along with samples PI11-X8, PI07-X10, PI03-X4, which were all rejected from the final mean D and I calculations.

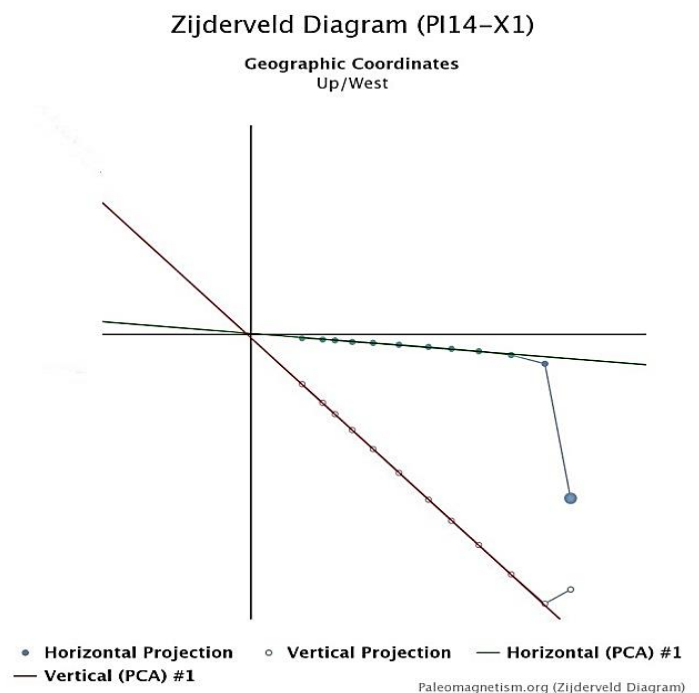


Figure 4.4.4 E.g. Zijdeveld diagram from PI14- X1 with a change in magnetisation after the first de-magnetisation step.

Measured and Reference Geomagnetic Field Intensities for past 4ka, Azores

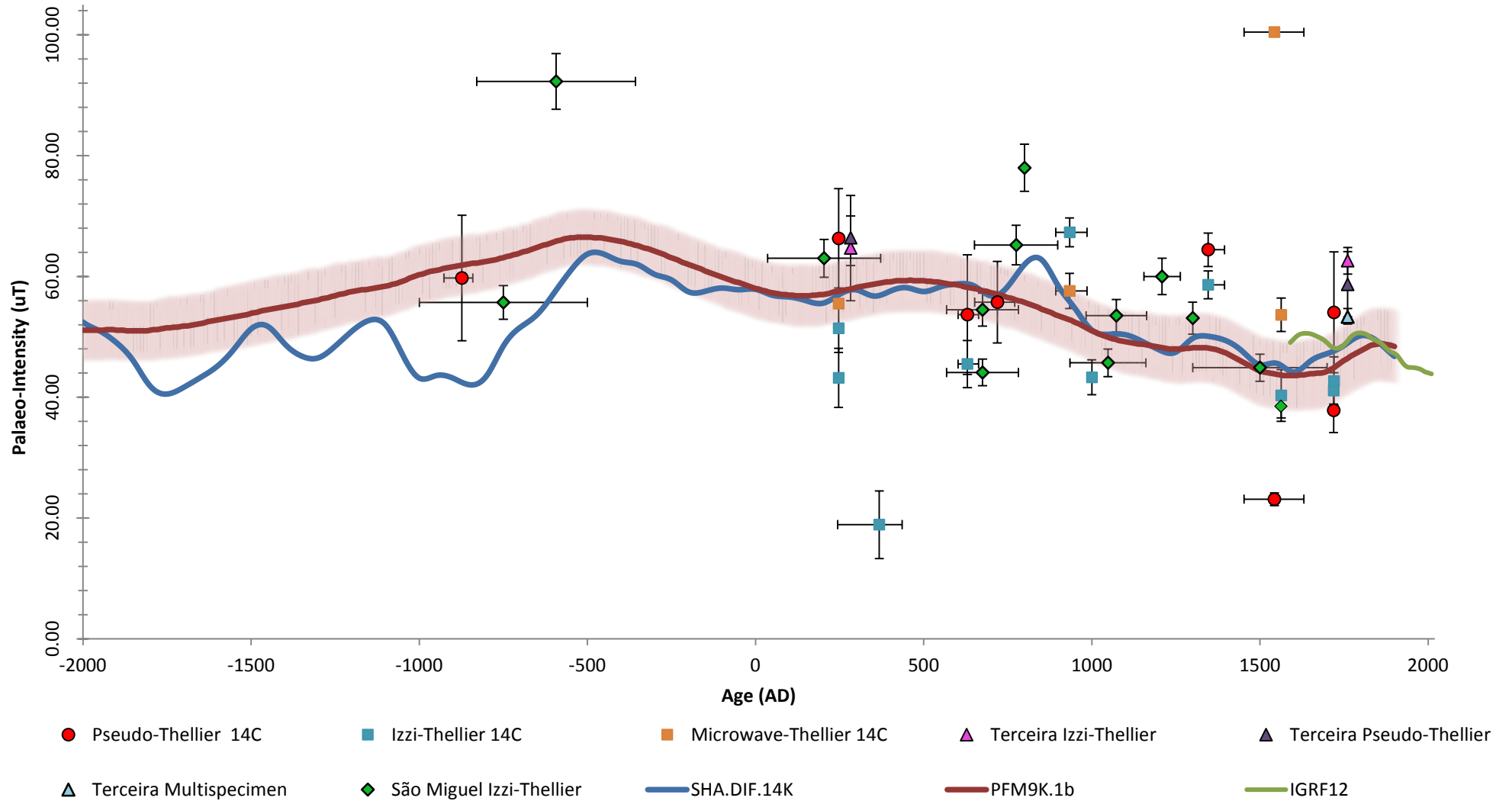


Figure 4.4.5 Final plot of achieved pTh PMI values paired with OSL ages (red circles), with results from neighbouring islands of Terceira (de Groot, et al., 2016), and Sao Miguel (Di Chiara, et al., 2014) and from the BSc thesis of van Grinsven, (2016) and Gülcher (2016). Reference geomagnetic field models are also plotted with the radiocarbon ages. The shading indicates 1σ confidence bands.

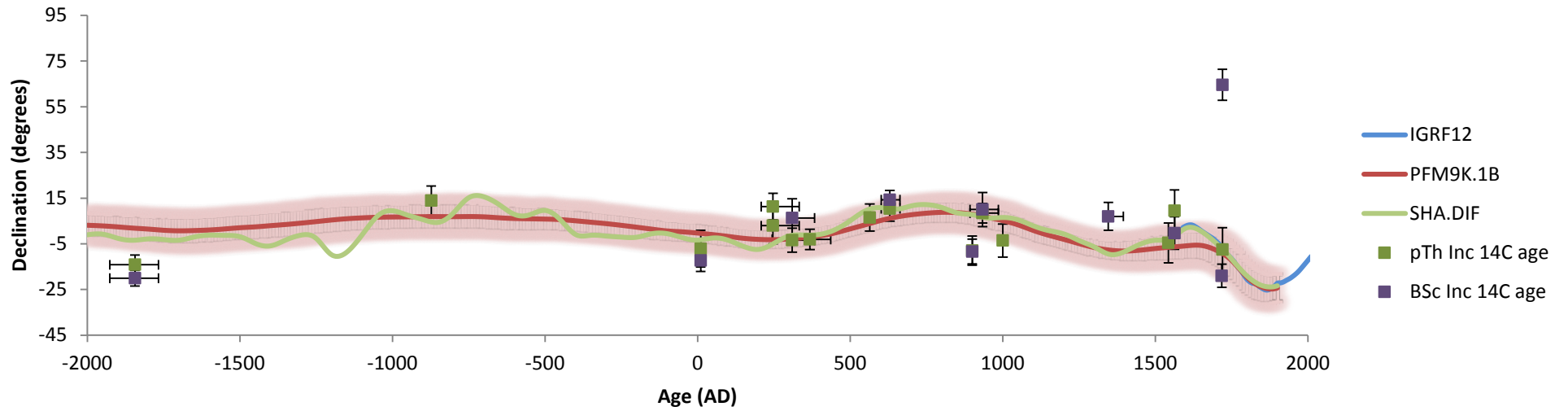
The equal area projection plots were supportive of the evaluations of the Zijderveld diagrams, with few samples showing any wandering behaviour. PI-14 again produced the most unusual behaviour with some directional alterations seemingly to have taken place.

The results of the directional data are summarised in Table 4.4.2. Out of the averaged 21 inclination and declination values, 15 of these passed the dispersion (k) criteria, with k values between 60.23 and 250.64. One sample had incredibly high K value of 1123.5, indicative of localised directional behaviour and was also rejected. The α_{95} confidence values are also $>10^\circ$ for the samples failing the k criteria, except from PI-04 which has a very low value at 2° . The declination values were plotted with the ^{14}C ages and almost all lie within the confidence band of the PMF9K.1b model, with excellent consistency with the results obtained from Wassing, (2016) which show very similar values and a tight fit to the models (Figure 4.4.6). The same can almost be said for the inclination data, with the pTh and the BSc data (Wassing, 2016) following the trend of the PFM9K.1B model, but falling slightly below the model average between ~750-1600AD. This consistency with the geo-reference models and results from the conventional PMI methods, highlights the appropriateness of application of the pseudo-Thellier method for producing directional data.

Site Name	mDec (°)	mInc (°)	N	k	$\alpha_{95}(\circ)$
PI-11	14.88	48.00	4	12.56	26.99
PI-03	12.65	73.41	6	20.98	14.97
PI-05	6.26	27.22	6	35.31	11.43
PI-09	17.47	43.71	6	42.02	10.46
PI-02	356.85	41.40	6	43.37	10.29
PI-13	355.41	41.04	6	60.23	8.70
PI-22	6.49	56.83	6	69.82	8.07
PI-01	9.44	56.91	5	70.44	9.18
PI-20	352.87	32.65	6	71.87	7.96
PI-10	356.42	38.67	6	86.23	7.26
PI-07	352.52	67.80	4	92.79	9.59
PI-14	13.87	56.55	6	110.51	6.40
PI-18	2.93	55.94	6	111.21	6.38
PI-17	11.32	62.17	6	133.98	5.81
PI-15	10.37	56.16	6	148.56	5.51
PI-06	356.60	54.09	6	163.07	5.26
PI-19	345.83	56.14	5	165.23	5.97
PI-12	356.92	55.91	6	228.65	4.44
PI-16	8.40	37.27	6	246.39	4.28
PI-21	351.97	32.83	6	250.64	4.24
PI-04	341.35	63.63	6	1123.50	2.00

Table 4.4.2 Summary table of magnetic declinations and inclinations achieved from the pTh NRM demagnetisation data. Accepted data is in black, rejected value ($k < 50$ or >1000) are in blue.

pTh and BSc Declination & ¹⁴C Age



pTh and BSc Inclination & ¹⁴C Age

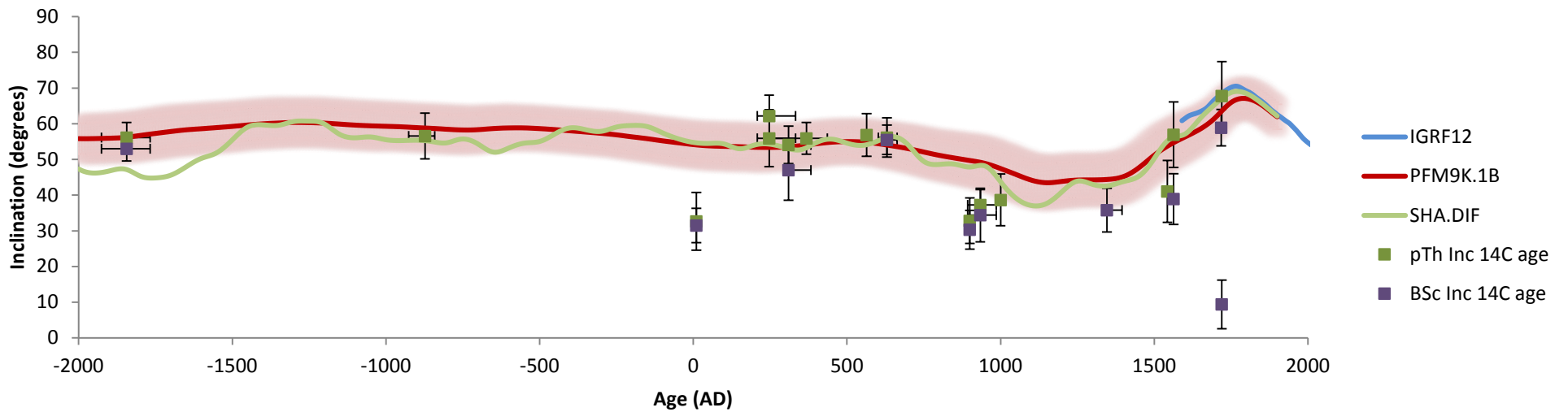


Figure 4.4.6 A) Declination from this study and the BSc thesis from Wassing, (2016), with 3 reference models. B) Inclination data with reference models. Vertical errors show α_{95} errors, and horizontal errors are 1σ probability intervals from the Radiocarbon calibration.

4.5 Discussion

With 8 absolute PMI values, and 15 directional values from the Pseudo-Thellier protocol, it is clear the method for absolute PMI determination is appropriate for the Pico basalts with the data constrained with the ^{14}C ages over the past 3ka. The samples evidently constituted appropriate mineralogy and magnetic properties, with relatively steady field intensities between 50-64 μT , and one significant decrease to 23.1 μT at 1543 AD (PI-13), which still fits within the ranges of the reference models.

With the Arai-style plots almost all showing stable magnetisation of the vectors, all absolute PMI values were calculated with at least 4 consecutive data points. This linearity and with high R^2 values, consistency in the magnetic minerals which underwent the de- and re-magnetisation stages is evident. Irregular relationships would be seen if different minerals were undergoing the magnetisation. Only PI-19 showed strange behaviour (see Figure 4.4.1), with a supposed linear demagnetisation for the first 5-6 steps. This is assumed to be a mistake in the files for this sample, with a mis-matching of the data and not an anomalous measurement result as not questionable directional or domain behaviour was seen.

There was good consistency between the samples per location, indicating good reliability and reproducibility in the results. All final PMI values were averaged over 3-7 samples, and sample PI-05 had an averaged PMI using only 2 samples but with a low standard deviation of 2.76 μT so was still included. The grouping of PI-03 and PI-04 initially presented an average of 55.1 μT and a sigma of 29.6, with two samples presenting incredibly high values of 97.1 and 99.5 μT from PI-03 which were removed from the final PMI calculation, lowering the sigma and presenting the accepted result. There is no discernible reason for these incredibly high values from PI-03, with no strange behaviour seen from the VSM or directional results, and are most likely due to heterogeneity in the magnetic minerals between the samples.

Compared to the IZZI-Thellier and Microwave Thellier results, the pTh results produced higher intensity values and slightly larger errors. The sigma values for the corresponding IZZI- and Microwave-Thellier age groups are all <5.6 μT compared to the grouped pTh standard deviations which have a peak at 10.4 μT . The final pTh PMI values are also relatively consistent with the reference intensity models. Whilst generally over estimating the models' average, the pTh values do roughly follow the peaks and troughs in intensity, with a general intensity decline between 500-1500AD. However, it should not be considered that the reference intensity models are 100% representative of the absolute PMI record, each with their own confidence bands and different resolutions. With many of the data points from the pTh and the other studies deviating away from the model, it cannot be said that these are incorrect as the geomagnetic intensity record can never be absolutely known or recreated.

From the directional data there was little sign of overprinting or alteration to the primary NRM in the samples. Several samples did plot directional vectors in different quadrants, which could be indicative of the sample being from a different lava unit with different magnetic properties, but any variations in direction are here put as random errors during the manual preparation of the samples. The sampling method aimed at ensuring homogeneity between collected cores, and it is unlikely that a different unit was sampled unknowingly. Only sample PI-14 showed any seemingly altered magnetic components but with accepted K and α_{95} values, it was included in the final directional results. The behaviour of this cannot be explained by my observations with no strange hysteresis properties seen in the VSM results.

From the rejected directional data (k values <50 and >1000) there was one sample (PI-04) which showed very discrete behaviour with a k value of 1123.5. Such a high value indicates very little dispersion in the data, which could indicate a localised magnetic characteristic, produced possibly from localised physical, chemical or thermal alteration, from other lava flows or hydrothermal fluids changing the magnetic moments. PI-04 did not show any strange behaviour in the plotted directional data or any notably high or low PMI value, but did produce the anomalous point in the Day plot, showing multi-domain properties, and thus the localised behaviour may be determined by specific mineralogy, with low coercivities and low saturation levels in different grains.

The analytical methods used for the Pseudo-Thellier PMI and directional results are deemed appropriate, with good visualisation of the NRM and ARM stages in the Excel Macro and from the paleomagnetism.org website indicating any anomalous behaviour. Easy selection of the linear components and reprocessing of results enables fast and clear results.

The island of Pico was selected to try to see any effects that the SAMA may have imparted on to the magnetic signals from these lava flows. The achieved PMI values are higher than the SAMA's average total intensity, with only one intensity dip to 23 μT around 1543 (PI-13) which may correspond to the wandering of the magnetic anomaly to the north, closer to Pico, but otherwise, any effects of the SAMA are not obvious.

These results show that the Pseudo-Thellier method is appropriate for full-vector quantification, with the PMI values corresponding well with other data sets and the directional vector data corresponding to the results of Wassing, (2016), indicating the Pseudo-Thellier method is highly suitable for determining such characteristics, with high reliability. Consistent primary natural remnant magnetic moments were recorded with few signs of overprints and no risk of thermal alteration.

5. Synthesis and discussion

5.1 Synthesis

Outlined here is a combining of the mineralogy and petrology findings in regards to the OSL and pseudo-Thellier results to answer the research aims in this study. Below is a summary (Table 5.1.1) of all OSL and pTh results, with calibrated ages and notes on mineralogy and petrology, followed by plots combining the gathered results and a thorough discussion.

The mineralogical and petrological assessments indicated the samples were all compositionally similar basalts, with the main variations between groundmass grain sizes and phenocryst phases. Only half of the samples had plagioclase phenocrysts present which are here considered a main contributor of primary emission centers. All measured feldspars were Ca-rich with >50% Anorthite which are not the most ideal for luminescence as such feldspars suffer from high fading rates, with high crystal disorder contributing to this, but all samples did have abundant magnetic minerals suitable for the pseudo-Thellier measurements constituting an estimated 18% of the groundmasses. The abundance of feldspars enabled dating the volcanic feldspars from the three main samples, using IRSL₅₀ SAR sequences on the 4-11 µm grain size fraction was achieved using a small data set with only 14% of aliquots producing De's used for dating. Two median ages were calculated falling close to their independent validation ages, within errors; PI-12 at 1.55 ± 0.49 ka, close to the 1.65 ¹⁴C age. PI-19 was dated at 3.05 ± 1.19 ka, also overlapping its 3.86 ka ¹⁴C age. PI-07 was dated at 2.64 ± 0.41 ka, overestimating the validation age of 0.3 ka. Characterisation of the luminescence signals was difficult with difficult mineralogy leading to inconsistent results and high sensitivity to regenerative doses with some De values calculated through extrapolation to unnaturally high values in response to high lab doses. These De's had to be statistically filtered to reduce skewness in the data. Some natural and regenerated decay curves were observed, but most were dominated by noise. No ages from the four 'other' basalts were achieved, and cannot be compared to their ¹⁴C ages or the Pico samples.

The Pseudo-Thellier approach produced 8 absolute palaeo-intensity values, consistent with other PMI values gained from conventional methods on the same samples, as well as with the reference models where the data points can be seen to follow the general curve of the reference geomagnetic field. All samples produced results representative of primary NRM's with no evidence of alteration or overprinting by thermal or chemical processes.

Only one of the pseudo-Thellier results could be paired with one OSL age, which was PI-07 with its over-estimated age. Figure 5.1.1 shows this pairing, and it is noted that the PMI value still falls coinciding with the geo-magnetic reference models. As the IRSL₅₀ weighted mean and median ages are similar despite the small data set, and the PMI and directional data also shows no strange behaviour, there data for this sample is seemingly reliable, and may indicate measurement of older

material entrapped within the lava unit. The $IRSL_{50}$ ages from PI-07 and PI-12 were also paired with the PMI values from the IZZI-Thellier results (Gülcher, 2016).

The pTh directional results were also considered precise with the obtained declination (D) and inclination (I) values fitting well within confidence intervals of the geo-magnetic reference models and with the results of Wassing, (2016). The D and I values for PI-07, -12 and -19 were constrained with the OSL ages (Figure 5.1.2), with all 3 points falling within confidence bands of the geomagnetic reference models. Considering the magnetic minerals and the results obtained here, the few EDS measurements showed low-Ti contents relative to their Fe contents, indicating the grains possibly have high saturation levels (Tauxe, et al., 2016/17) presenting them as appropriate for PMI determination.

Sample ID	14C Age (BP)	Calibrated age (AD) (1 σ , prob.)	Mineralogy/ petrology	Measured D _R (Gy/ka)	OSL Age (Ka)	pTh PMI Value (μ T)	Declination ($^{\circ}$) (α 95)	Inclination ($^{\circ}$) (α 95)
PI-04	298	1718	AVG 75.34% An MD			37.85 \pm 3.71		
PI-05	625 \pm 65	1346 (1341-1395, 0.608)	PSD			64.42 \pm 2.76		
PI-07	300	1720	AVG 64.86% An PSD	2.13 \pm 0.08	2.64 \pm 0.41	54.06 \pm 10.01	352.52 (9.59)	67.8 (9.59)
PI-11	1300 \pm 70	719 (652-771, 1.000)	AVG 72.00% An PSD			55.75 \pm 6.76		
PI-12	1680 \pm 115	368 (244-436, 0.756)	AVG 76.03% An PSD	2.08 \pm 0.08	1.55 \pm 0.49		356.92 (4.44)	55.91 (4.44)
PI-13	365 \pm 75	1543 (1453-1524, 0.502)	PSD			23.13 \pm 1.05	355.41 (8.70)	41.04 (8.70)
PI-14	2720 \pm 50	-873 (-905 - -820, 1.000)	PSD			59.74 \pm 10.39	13.87 (6.40)	56.55 (6.40)
PI-15	1405 \pm 50	630 (602-663, 1.000)	PSD			53.69 \pm 9.91	10.37 (5.51)	56.16 (5.51)
PI-17	1780 \pm 70	247 (208-333, 0.742)	PSD			66.30 \pm 8.23	11.32 (5.80)	62.17 (5.80)
PI-18	1780 \pm 70	247 (208-333, 0.742)	SD/PSD			66.30 \pm 8.23	2.93 (7.96)	55.94 (7.96)
PI-19	3520 \pm 60	-1844 (-1921 - -1762, 1.000)		1.76 \pm 0.07	3.05 \pm 1.19		345.83 (4.24)	56.14 (4.24)
HW-10	1470 \pm 50	588 (558-640, 1.000)		To low counts		44.2 \pm 2.5 (De Groot, et al., 2013)		
TER-18	1760 \pm 40	283 (209-384, 0.911)		5.77 \pm 0.20		66.4 (de Groot, et al., 2016)		
GCR-47	3030 \pm 90	-1266 (1406-1191, 0.912)		2.38 \pm 0.09			13.1 (19.2) (de Groot, et al., 2015)	42.9 (19.2) (de Groot, et al., 2015)
TF-6	3620 \pm 140	-1995 (2148-1865, 0.780)		3.76 \pm 0.13		38.1 \pm 4.4 (de Groot, et al., 2015)		

Table 5.1.1. Summary of all achieved IRSL₅₀ ages and Pseudo-Thellier PMI and directional results with corresponding calibrated radiocarbon ages. Average anorthite % from EDS measurements and the domain states from the VSM results are stated. PMI and/or directional values for the other four basalts are also provided from literature.

Paired OSL and Pseudo-Thellier results, Pico

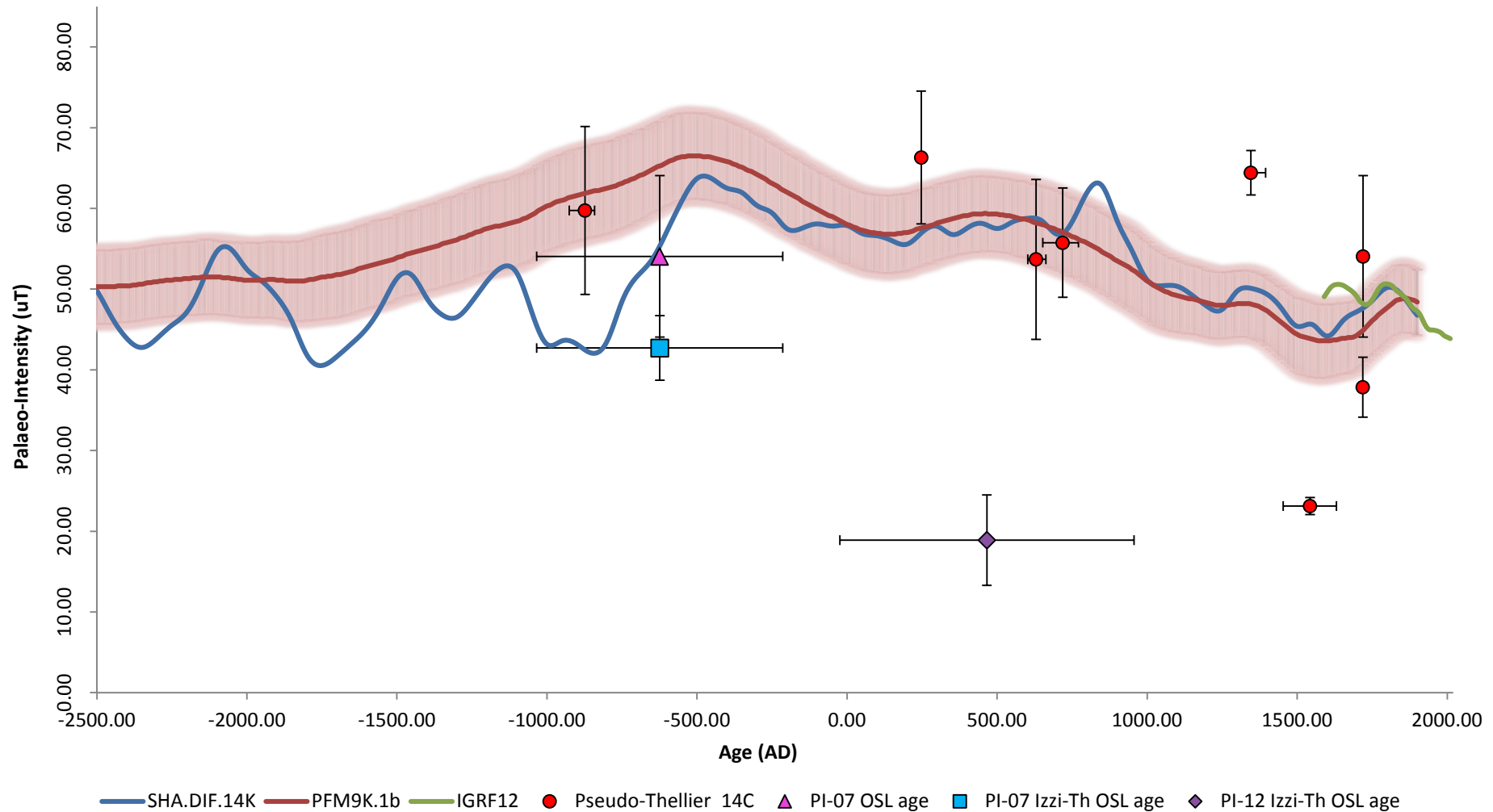
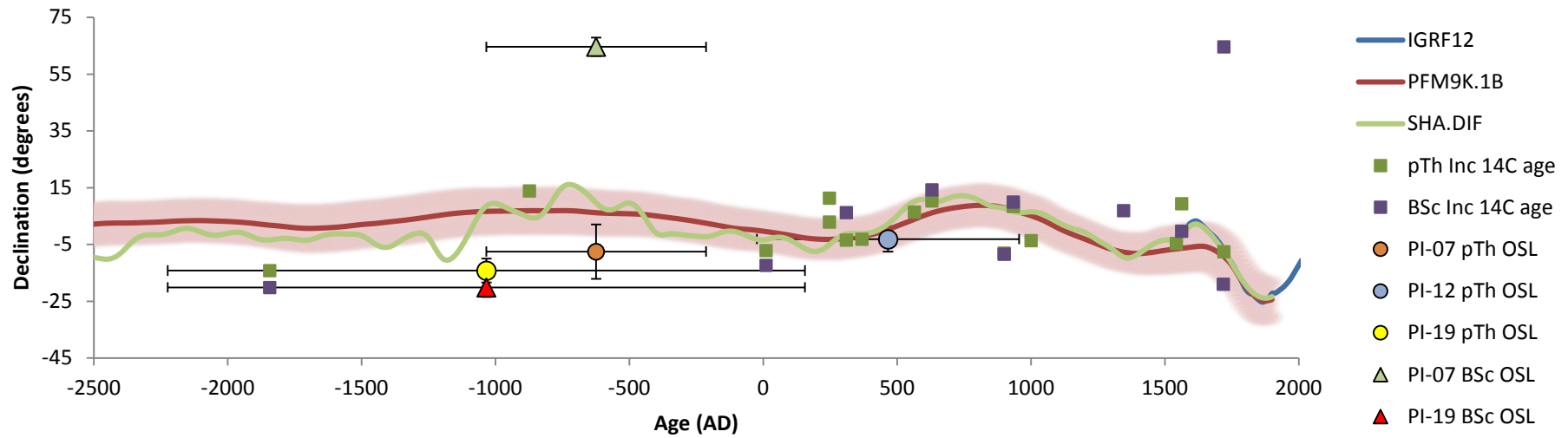


Figure 5.1.1. Palaeo-magnetic intensity changes over the past 3ka, from the Pseudo-Thellier measurements and calibrated 14C ages. Red and blue lines indicate reference geomagnetic field models SHA.DIF.14K, PFM9K.1b and IGRF12. Shading indicates 1 standard deviation confidence limits. The one paired OSL and pTh result is plotted (Pink triangle, PI-07 OSL age). The PI-07 and PI-12 OSL ages were also paired with results from the IZZI-Thellier tests (blue square and purple diamond).

OSL Ages paired with pTh and BSc Declination, Pico



OSL Ages paired with pTh and BSc Inclination, Pico

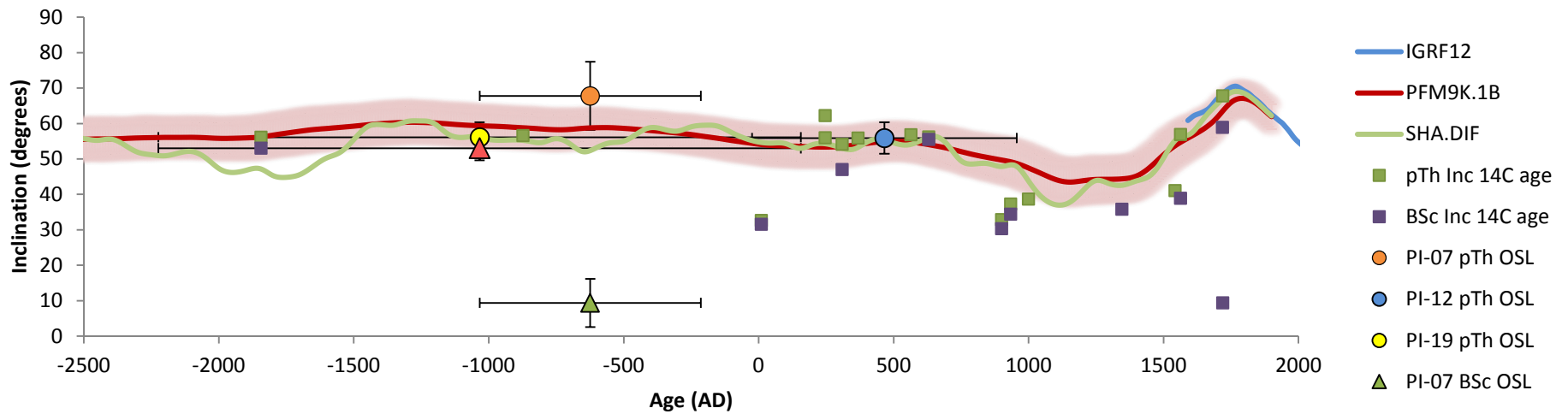


Figure 5.1.2 Top: OSL ages paired with pTh and the BSc results from Wassing, (2016), as well as all inclinations plotted over the calibrated radiocarbon ages. Bottom: Same as top but for Declination.

Discussion

Mineralogy, Petrology and Dose rate

Appropriate mineralogy must be present for producing measurable luminescence and magnetic signatures. From the thin section observations, only half of the samples had plagioclase phenocryst phases, with the majority of the feldspars in the groundmasses. It was considered there would be appropriate emission centres for the OSL measurements and the magnetic minerals for determining the palaeo-intensities.

There was a miss-matching of the estimated phenocryst abundance with the measured D_R values, with PI-19 estimated to have the highest abundance of feldspar phenocrysts at 40%, but producing the lowest measured D_R value at 1.76 ± 0.07 Gy/ka. This indicates that visual assessments of the mineral assemblages are not singularly appropriate for preliminary determination of dose rates or suitability for luminescence tests. Relating to the low dose rates are the results from the EDS which indicated low values for Potassium, with all samples ≤ 0.46 mass%. This possibly relates to the relatively low D_R values of 2.13, 2.08 and 1.76 Gy/ka for PI-07, -12 and PI-19 respectively, which fall on the lower end of the dose rates expected in nature of 2-3Gy/ky (Tsukamoto & Duller, 2008).

The dose rate measurements from the other four basalts were significantly variable compared to the Pico samples. A maximum of 5.77 ± 0.20 Gy/ka was achieved from the Terceira sample, significantly deviating from any of the Pico dose rates between 1.76 and 2.13 Gy/ka and suggests a different chemical composition and possibly a different mantle source, enriched in radioactive isotopes. For all D_R calculations, it must be noted that the sample depths were not known and set at 0 m, and the water content was set at an arbitrary $2 \pm 2\%$, both of which undoubtedly introduce unquantifiable error into the results. Further investigations should also be conducted into the effects of the SAMA on the contributing cosmic irradiation to the total dose rate, as the low strength of the field causes an increased level of cosmic nuclides to reach the Earth's surface. But considering Pico is in equatorial regions the strength of the magnetic field is already weaker than at the poles, and the effects of the SAMA are not believed to be large.

Samples PI-07 and PI-12 were found to have the highest ranges in Na and K contents from the EDS results. All measured samples with the EDS showed Ca-rich compositions with $>50\%$ Anorthite contents in all samples, classifying as Bytownite or Labradorite, and indicating that obtaining datable luminescence signals would most likely be difficult due to high fading rates.

Mineralogy, petrology and OSL

The absence of feldspar phenocrysts in many of the samples can instantly be tied to the poor OSL results. The three main samples all had feldspar phenocryst phases, with relatively coarser groundmasses compared to the other samples, which does indicate some relation between mineral sizes/phases and the suitability for OSL measurements. It does not however, explain the poor results

from the rest of the Pico samples, which all had ample feldspars in their groundmasses - up to an estimated 65%, which would logically have shown luminescence with at least one of the separated grain size fractions. There is believed to be a high level of disorder within the crystals, which crystallised quickly following high temperature eruption. This low degree of ordering is argued to be a main cause of few stable or deep traps and a contributor to a fading signal (Fattahi & Stokes, 2003). As the basalts from Pico were eruptive with observations of blurred lamellae in many crystals, this disorder may explain the lack of luminescence emissions from the groundmass feldspars, and the variation between samples and tests runs. As the natural luminescence was so dim for the samples here, the ages were not corrected for any possible fading using the calculated g-values.

The dim signals can be explained through addressing the EDS results for the feldspar compositions which had high calcium contents (>60% An) which is inhibiting for building and retaining stable luminescence signals as fading rates have been found to increase with >5% Ca content (Valla, et al., (2016); Huntley, et al., (2007). This overall high Ca content may lead to the signal fading during storage between tests, or cause the traps in the crystal lattices may be too shallow and unstable, accounting for the variable results. However, PI-07 and -12 had the highest ranges in K and Na content, which may explain why any results were achieved from this sample, with some aliquots having higher Na or K containing plagioclase than others. PI-19 had less compositional range but as it is the oldest flow, the crystals may have become more structurally ordered over time, enabling luminescence signal build up, suitable for dating.

During the test runs, there were instances of natural and regenerated signals. Whilst here the samples were given a huge irradiation dose compared to what is seen in nature, it did show the samples' capabilities' to actually build up and emit a recognisable feldspar emission, indicating that the samples may if older, be suitable for dating. Here the samples are most likely just too young or have too low surrounding irradiation dose rates for significant signal build-up in their geologically short <3ka lifetimes. It could be argued that there is a minimum D_R required to be able to have appropriate signal build up to be able to date such young deposits, but other works which have achieved ages from younger K-feldspars (<390 years) with smaller dose rates of $\leq 1.70 \pm 0.1$ Gy/ka (Reimann & Tsukamoto, 2012). With this and the dose rate from Terceira being high at 5.77 ± 0.20 Gy/ka and the complete lack of success at dating that sample with $IRSL_{50}$, it is evident that any lower-limit dose rate will vary between sample location, age and mineralogy and would be very hard to define.

Despite this, for sample PI-12 which had the high measured Na and K mass%, and the oldest sample PI-19 the $IRSL_{50}$ tests were successful at producing ages exactly comparable to the ^{14}C ages. With the PI-07 sample $IRSL_{50}$ age deviating from the validation age, possibly due to compositional variations in the minerals under scrutiny, and the lack of success at dating the other 7 highlight how slight differences in mineralogy and crystal abundance influence the success of the results. It is

suggested that performing even a quick mineralogical and chemical assessment on the samples before attempting OSL age determination could save time as the samples with the most appropriate chemical composition and mineral abundances can be selected. An alternative would be to investigate the different mineral contributions to the total luminescence signals which may indicate alternatives to feldspars or at least indicate what other emissions to avoid.

The IRSL₅₀ results from the other four samples (Hawaii, Terceira, Tenerife and Gran Canaria) were all noise dominated and un-datable. However, with the incredibly high D_R from the Terceira sample, it was surprising that no luminescence emission was detected. The samples' mineralogy may be hindering this signal build up or the storage time and sample collection methods may have led to the signal fading. With the samples from Gran Canaria and Tenerife, the dose rates were also considered suitable for building a luminescence signal, but again the sampling method and storage time may have hindered these results.

Pseudo-Thellier and OSL

Only one result from the Pseudo-Thellier measurements had a corresponding IRSL₅₀ age- PI-07 (Figure 5.1.1). The PI-12 and PI-07 IRSL₅₀ ages and the IZZI-Thellier PMI results from Gülcher, (2016) were also plotted, and the pTh declination and inclination results were also presented with their IRSL₅₀ ages (Figure 5.1.2).

With the plotted PI-07 OSL and pTh results, it is apparent that the PMI and directional data fit with the SHA.DIF.14K and PFM9K.1b reference models at this age. This sample corresponds to an eruption from 1720, and is believed to be from the same time as the eruption of the unit where PI-04 was collected (Figure 1.2.1), and it has been found that this PI-07 unit – and several other Pico lava flows- has older xenoliths and xenocrysts present throughout them (Mitchell, et al., 2008). The present results could indicate that the measurements were conducted on an older xenolith/xenocryst instead of the anticipated younger unit. The sample did have plagioclase phenocrysts (unlike PI-04) and the highest estimated olivine phenocryst content, at 60% of all phenocrysts which may be from coarser included xenocrysts, but with no other discernible differences (e.g. textures) observed, the IRSL₅₀ age may still just be inaccurate – assuming the ¹⁴C ages are correct. Further chemical and mineralogical assessments would provide a better answer as to the source of the measured material, as well as attempting to date sample PI-04 which, if it provided the expected 0.3 ka age, would support the suitability of the samples for providing suitable ages and support the idea that PI-07 is a sample from an older inclusion and thus the older IRSL₅₀ age is appropriate.

The IRSL₅₀ and Pseudo-Thellier results are suitable for combining, with measurements taken on the same material which was sampled in a way to maximise homogeneity between the cores. With the success of applying the pTh method here and by de Groot, et al. (2016) and previous works on volcanic K- feldspars producing datable, high count decay curves, it is clear there is the possibility for

reliable absolute dating and palaeo-intensity measurements on samples <3ka, but appropriate mineralogy for stable signal growth and possibly a minimum dose rate must be present.

Whilst the proximity of the Azores to the SAMA was here considered suitable, there was little evidence of the SAMA influencing the magnetic signatures in the Pico basalts, with generally higher PMI values than what is found at the anomaly. There is still a need to address the anomaly at closer proximity and at higher resolution for a complete documentation and understanding.

Mineralogy, petrology and Pseudo-Thellier

The VSM measurements are a standard practice accompanying Pseudo-Thellier measurements, using hysteresis properties governed at least in part by grain size for indicating reliability within the results. The samples consisted of a mix of single and multi-domain minerals, which fit along the SD and MD theoretical mixing curve for magnetite (Dunlop, 2002) which are desirable for PMI measurements. There was no relation between hysteresis properties and sample age, which indicates little mineral growth and splitting of domains due to external heating by younger flows. Sample PI-04 was the only sample which presented multi-domain properties, but no strange behaviour was seen in the PMI or directional data and therefore it is considered the sample contained enough appropriate magnetic minerals which did successfully capture the characteristics of the EMF at time of formation. This is another difference between PI-07 and PI-04 where PI-07 presented PSD grains, with higher coercivities and magnetic saturation levels than PI-04.

Too few EDS measurements were taken to fully discuss the mineralogy alongside the pTh results, but the observations with the polarising microscope indicate the relatively high abundance of opaque magnetic minerals (estimated at $\leq 30\%$ of the groundmass for all samples), with even some lineation structures and mineral clusters, which promote the samples' suitability for measurement with the Pseudo-Thellier method.

5.2 Conclusion

The aims of this study were met, constraining the characteristics of the Earths' magnetic field over the past 3 ka of the Holocene using Ca-rich feldspars and magnetic minerals from basalts from the Island of Pico. Using luminescence protocols outlined by Tsukamoto, et al, (2011), charactering TL, BLSL and pIRIR emissions from the feldspars was difficult, with all samples producing dim and noisy natural and regenerated emissions. IRSL₅₀ was the best protocol for these samples, but only 14% of all measured aliquots were successful at producing De's suitable for age calculation.

Three samples were dated with IRSL⁵⁰ at 1.64 ± 0.41 ka (PI-07), 1.55 ± 0.49 ka (PI-12) and 3.05 ± 1.19 ka (PI-19), with PI-12 and -19 overlapping their ¹⁴C ages of 1.65 and 3.86 ka respectively (Nunes, 1999). The PI-07 IRSL₅₀ age overestimates the 0.3 ka ¹⁴C validation age. A total of 8 PMI values ranging between 23.1-64.4 μ T were achieved using the Pseudo-Thellier palaeo-intensity method (De Groot, et al., 2013), all of which are consistent with the results from IZZI-Thellier (Gülcher, 2016), Microwave-Thellier (Van Grinsven, 2016) tests, as well as with geo-magnetic reference models (IGRF12, PFM9K.1b and SHA.DIF). Only PI-07 could pair its IRSL₅₀ age with the achieved PMI value of 54.06 ± 10.01 , and when plotted, the PMI values still falls within confidence bands of the reference models, and the age overestimation could be due to mistakenly sampling and dating a xenolith or older inclusion which are known to be present throughout this lava unit and would explain the older age. The IRSL₅₀ ages for PI-12 and PI-19 were paired with corresponding PMI results from the IZZI-Thellier (Gülcher, 2016) and Microwave-Thellier (Van Grinsven, 2016) studies and also fit within model confidence bands.

The mineralogy of the feldspars was not favourable, with high Ca contents (>50% An) leading to presumed high fading rates and dim natural signals. Low internal potassium in the feldspars negatively influencing the total dose rates which were reasonably low at $1.76 \pm 0.07 - 2.13 \pm 0.08$ Gy/ka. The magnetic minerals all showed pseudo-single domain properties, except PI-04 which showed higher susceptibility and lower natural remnant coercivity than the other samples.

In light of these results it is clear there is need for thorough mineralogical assessment of the material in question prior to dating, with the success of luminescence dating governed by the internal mineralogy, which here led to noisy and few usable results. The luminescence methods used here have been successfully applied to older materials, and a minimum age limit of ~1 ka could be argued for achieving accurate and replicable results from Ca-rich volcanic feldspars, but there must be a smoothing of the protocols to date such materials. The results here support the use of IRSL₅₀ dating methods on volcanic feldspars ≤ 3 ka, alongside or in place of ¹⁴C or other dating methods. These ages constrained the results from the Pseudo-Thellier method for palaeo-magnetic intensity determination

which were performed on the same material, and both methods should be explored further to increase the resolution of the current palaeo-magnetic intensity record.

Acknowledgements

I would like to express my sincere appreciation to my tutors and supervisors who have introduced and then launched me into two brand new topics I previously knew nothing about. Thank you, it's been fun! Sincere gratitude also to Alice and Erna, who taught me and helped me with lots of lab work, I hope you also enjoyed it! And with all the thanks and love to my family and friends, who probably have no idea what I am talking about half of the time, you are always supportive with everything I am doing.

Bibliography

- Ademola, J. A., 2014. Luminescence Characteristics of Feldspar from Nigeria. *Natural Science*, 28 2, Volume `6, pp. 1-7.
- Auclair, M., Lamothe, M. & Huot, S., 2003. Measurement of anomalous fading for feldspar IRSL using SAR. *Radiation measurements*, 37(4), pp. 487-492.
- Beier, C., Haase, K. M. & Turner, S. P., 2012. Conditions of melting beneath the Azores. *Lithos*, Volume 144, pp. 1-11.
- Bøtter-Jensen, L., Andersen, C. E., G. A. T. Duller & Murray, A. S., 2003. Developments in radiation, stimulation and observation facilities in luminescence measurements. *Radiation Measurements*, 37(4), pp. 535-541.
- Bowen, N. L., 1922. The reaction principle in petrogenesis. *The Journal of Geology*, 30(3), pp. 177-198.
- Butler, R. F., 1998. *Paleomagnetism: Magnetic Domains to Geologic Terrane*. Electronic ed. Portland: s.n.
- Calvert, A. T., Moore, R. B., McGeehin, J. P. & da Silva, A. M. R., 2006. Calvert, A. T., Moore, R. B., McGeehin, J. P., & da Silva, A. M. R. (2006). Volcanic history and 40 Ar/39 Ar and 14 C geochronology of Terceira Island, Azores, Portugal. *Journal of Volcanology and Geothermal Research*, 156(1), pp. 103-115.
- Chen, Y. et al., 2015. Maximum age limitation in luminescence dating of Chinese loess using the multiple-aliquot MET-pIRIR signals from K-feldspar. *Quaternary Geochronology*, pp. 207-212.
- Collinson, D. (., 2013. *Methods in rock magnetism and palaeomagnetism: techniques and instrumentation*. Illustrated ed. s.l.:Springer Science & Business Media..
- Cunningham, A., Wallinga, J. & Minderhoud, P., 2011. Expectations of scatter in equivalent-dose distributions when using multi-grain aliquots for OSL dating. *Geochronometria*, 38(4), pp. 424-431.
- Day, R., Fuller, M. & Schmidt, V. A., 1977. Hysteresis properties of titanomagnetites: grain-size and compositional dependence. *Physics of the Earth and planetary interiors*, 13(4), pp. 260-267.
- de Groot, L. et al., 2015. High paleointensities for the Canary Islands constrain the Levant geomagnetic high. *Earth and Planetary Science Letters*, Volume 419, pp. 154-167.
- De Groot, L. et al., 2013. Rapid regional perturbations to the recent global geomagnetic decay revealed by a new Hawaiian record. *Nature communications*, Volume 4.
- de Groot, L. V., Pimentel, A. & Di Chiara, A., 2016. The multimethod palaeointensity approach applied to volcanics from Terceira: full-vector geomagnetic data for the past 50 kyr. *Geophysical Journal International*, 206(1), pp. 590-604.
- Di Chiara, A., Tauxe, L. & Speranza, F., 2014. Paleointensity determination from São Miguel (Azores Archipelago) over the last 3ka. *Physics of the Earth and Planetary Interiors*, Volume 234, pp. 1-13.
- Duller, G. A. T., 2015. The Analyst software package for luminescence data: overview and recent improvements. *Ancient TL*, 33(1), pp. 35-42.
- Dunlop, D. J., 1979. On the use of Zijderveld vector diagrams in multicomponent paleomagnetic studies. *Physics of the Earth and Planetary Interiors*, 20(1), pp. 12-24.
- Dunlop, D. J., 2002. Theory and application of the Day plot (Mrs/Ms versus Hcr/Hc) 1. Theoretical curves and tests using titanomagnetite data. *Journal of Geophysical Research: Solid Earth*, Volume 107.
- Fattahi, M. & Stokes, S., 2003. Dating volcanic and related sediments by luminescence methods: a review. *Earth-Science Reviews*, pp. 229-264.
- França, Z. T. et al., 2006. Petrology, geochemistry and Sr–Nd–Pb isotopes of the volcanic rocks from Pico Island—Azores (Portugal). *Journal of Volcanology and Geothermal Research*, 156(1), pp. 71-89.
- Franke, C. et al., 2007. Identification of magnetic Fe-Ti oxides in marine sediments by electron backscatter diffraction in scanning electron microscopy. *Geophysical Journal International*, Volume 170, pp. 545-555.

- Goldstein, J. et al., 2012. *Scanning electron microscopy and X-ray microanalysis: a text for biologists, materials scientists, and geologists*. 2, illustrated ed. s.l.:Springer Science & Business Media..
- Gomez-Paccard, M. et al., 2012. Improving our knowledge of rapid geomagnetic field intensity changes observed in Europe between 200 and 1400 AD. *Earth and Planetary Science Letters*, Volume 355, pp. 131-143.
- Graham, D. J. & Midgley, N. G., 2000. Technical Communication-Graphical Representation of Particle Shape using Triangular Diagrams: An Excel Spreadsheet Method.. *Earth Surface Processes and Landforms*, 25(13), pp. 1473-1478.
- Grootes, P. M., 2015. Radiocarbon: Clock and tracer. *Encyclopedia of Marine Geosciences*, pp. 1-7.
- Guérin, G. et al., 2012. On the use of the infinite matrix assumption and associated concepts: a critical review. *Radiation Measurements*, 47(9), pp. 778-785.
- Gülcher, J., 2016. *Obtaining a high-resolution geomagnetic field intensity record for the Azores region The IZZI-Thellier approach*. BSc Thesis, Utrecht: Utrecht University.
- Guralnik, B. et al., 2015. OSL-thermochronometry using bedrock quartz: A note of caution. *Quaternary geochronology*, Volume 25, pp. 37-48.
- Hartmann, G. A. & Pacca, I. G., 2009. Time evolution of the South Atlantic magnetic anomaly.. *Anais da Academia Brasileira de Ciências*, 81(2), pp. 243-255.
- Huntley, D. J., 2006. An explanation of the power-law decay of luminescence. *Journal of Physics: Condensed Matter*, 18(4), p. 1359.
- Huntley, D. J., B. M. R. & Haidar, S., 2007. Tunnelling in plagioclase feldspars.. *Journal of Physics D: Applied Physics*, 40(3), p. 900.
- IGRF, 2014. NOAA. [Online]
Available at: <https://www.ngdc.noaa.gov/IAGA/vmod/igrf.html>
[Accessed 16 03 2017].
- Jackson, A., Jonkers, A. R. & Walker, M. R., 2000. Four centuries of geomagnetic secular variation from historical records.. *Philosophical Transactions of the Royal Society of London A: Mathematical, Physical and Engineering Sciences*, Volume 358, pp. 957-990.
- Koymans, M. R., Langereis, C. G., Pastor-Galán, D. & van Hinsbergen, D. J., 2016. *Paleomagnetism.org: An online multi-platform open source environment for paleomagnetic data analysis*. [Online]
Available at: <http://www.paleomagnetism.org>
[Accessed 14 02 2017].
- Kruiver, P. P. et al., 1999. A pseudo-Thellier relative palaeointensity record, and rock magnetic and geochemical parameters in relation to climate during the last 276 kyr in the Azores region. *Geophysical Journal International*, 136(3), pp. 757-770.
- Lemoine, J. M. & Capdeville, H., 2006. A corrective model for Jason-1 DORIS Doppler data in relation to the South Atlantic Anomaly. *Journal of Geodesy*, 80(8-11), pp. 507-523.
- Li, B., Jacobs, Z., Roberts, R. G. & Li, S. H., 2014. Review and assessment of the potential of post-IR IRSL dating methods to circumvent the problem of anomalous fading in feldspar luminescence.. *Geochronometria*, 41(3), pp. 178-201.
- Lohmann, K. J. et al., 2004. Animal behaviour: geomagnetic map used in sea-turtle navigation.. *Nature*, Volume 428, pp. 909-910.
- Lowrie, W., 2007. *Fundamentals of Geophysics*. 2 ed. Cambridge: Cambridge University Press.
- McDougall, I. & Schmincke, H. U., 1976. Geochronology of Gran Canaria, Canary Islands: age of shield building volcanism and other magmatic phases. *Bulletin of Volcanology*, 40(1), pp. 57-77.
- Métrich, N. Z. V. C. L. H. A. M. M. & M. F. O., 2014. Is the 'Azores hotspot' a wet spot? Insights from the geochemistry of fluid and melt inclusions in olivine of Pico basalts. *Journal of Petrology*, 55(2), pp. 377-393.
- Miranda, J. et al., 1998. Tectonic setting of the Azores Plateau deduced from a OBS survey. *Marine Geophysical Researches*, 20(3), pp. 171-182.

- Mitchell, N. C. et al., 2008. Lava penetrating water: Submarine lava flows around the coasts of Pico Island, Azores. *Geochemistry, Geophysics, Geosystems*, 9(3).
- Nesse, W. D., 2000. *Introduction to Mineralogy*. Oxford: Oxford University Press.
- NGDC, N., 2016. *Further Understanding of Geomagnetism*. [Online] Available at: <https://www.ngdc.noaa.gov/geomag/geomaginfo.shtml> [Accessed 26 03 2017].
- Nunes, J. C., 1999. A actividade vulcânica na ilha do Pico do Plistocénico Superior ao Holocénico: mecanismo eruptivo e hazard vulcânico. *Provas de Doutoramento*.
- Panzeri, L., Martini, M. & Sibilia, E., 2012. Effects of thermal treatments on luminescence features of three natural feldspars. *Radiation Measurements*, 47(9), pp. 877-882.
- Preusser, F. et al., 2008. Luminescence dating: basics, methods and applications. *Quaternary Science Journal*, Volume 57, pp. 95-145.
- Prytulak, J. & Elliott, T., 2009. Determining melt productivity of mantle sources from ^{238}U – ^{230}Th and ^{235}U – ^{231}Pa disequilibria; an example from Pico Island, Azores. *Geochimica et Cosmochimica Acta*, 73(7), pp. 2103-2122.
- Quartau, R. et al., 2015. The insular shelves of the Faial-Pico Ridge (Azores archipelago): A morphological record of its evolution. *Geochemistry, Geophysics, Geosystems*, Issue 16, pp. 1401-1420.
- Reimann, T., Ankjærgaard, C. & Wallinga, J., 2015. Testing the potential of a transferred IRSL (T-IRSL) feldspar signal for luminescence dating. *Radiation Measurements*, Volume 81, pp. 275-281.
- Reimann, T. & Tsukamoto, S., 2012. Dating the recent past (< 500 years) by post-IR IRSL feldspar—Examples from the North Sea and Baltic Sea coast. *Quaternary Geochronology*, Volume 10, pp. 180-187.
- Reimer, P. et al., 2013. IntCal13 and Marine13 radiocarbon age calibration curves 0-50,000 years cal BP. pp. 1869-1887.
- Schettino, A. & Scotese, C. R., 2005. Apparent polar wander paths for the major continents (200 Ma to the present day): a palaeomagnetic reference frame for global plate tectonic reconstructions. *Geophysical Journal International*, 163(2), pp. 727-759.
- Shah, J. et al., 2016. Palaeomagnetic evidence for the persistence or recurrence of geomagnetic main field anomalies in the South Atlantic. *Earth and Planetary Science Letters*, Volume 441, pp. 113-124.
- Tarduno, J. A. C. R. D. W. M. K. & B. D., 2007. Geomagnetic field strength 3.2 billion years ago recorded by single silicate crystals. *Nature*, Volume 446, pp. 657-660.
- Tauxe, L., Banerjee, S., Butler, R. & van der Voo, R., 2016/17. *Essentials of Paleomagnetism, 4th Web Edition*. [Online] Available at: <https://earthref.org/MagIC/books/Tauxe/Essentials/> [Accessed 2017].
- Tauxe, L., Pick, T. & Kok, Y. S., 1995. Relative paleointensity in sediments: a pseudo-Thellier approach. *Geophysical Research Letters*, 22(21), pp. 2885-2888.
- Thellier, E. & Thellier, O., 1959. On the Intensity of the Earth's Magnetic Field in the Historical and Geological Past. *Izv. Akad. Nauk SSSR, Ser. Geofiz*, Volume 9, pp. 1296-1331.
- Tsukamoto, S. & Duller, G. A. T., 2008. Anomalous fading of various luminescence signals from terrestrial basaltic samples as Martian analogues. *Radiation Measurements*, 43(2), pp. 721-725.
- Tsukamoto, S., Duller, G. A. T., Wintle, A. G. & Muhs, D., 2011. Assessing the potential for luminescence dating of basalts. *Quaternary Geochronology*, 6(1), pp. 61-70.
- Tsukamoto, S. et al., 2014. Luminescence dating of scoria fall and lahar deposits from Somma-Vesuvius, Italy. *Quaternary Geochronology*, Volume 20, pp. 39-50.
- Valla, P. G. et al., 2016. Valla, P. G., Lowick, S. E., Herman, F., Champagnac, J. D., Steer, P., & Guralnik, B. *Quaternary Geochronology*, pp. 55-66.

Van Grinsven, L., 2016. *Expanding the full-vector geomagnetic record for Pico island (the Azores) using the Microwave Thellier approach*. BSc Thesis, Utrecht: Utrecht University.

Wang, D. & Van der Voo, R., 2004. The hysteresis properties of multidomain magnetite and titanomagnetite/titanomaghemite in mid-ocean ridge basalts. *Earth and Planetary Science Letters*, 220(1), pp. 175-184.

Wassing, F., 2016. *Paleodirections of Pico Island: reconstructing the past 3000 years*. BSc Thesis, Utrecht: Utrecht University.

Wintle, A. G., 1977. Detailed study of a thermoluminescent mineral exhibiting anomalous fading. *Journal of Luminescence*, 15(4), pp. 385-393.

Wintle, A. G., 2008. Luminescence dating: where it has been and where it is going. *Boreas*, 37(4), pp. 471-482.

Yu, Y., Dunlop, D. J. & Özdemir, Ö., 2003. Are ARM and TRM analogs? Thellier analysis of ARM and pseudo-Thellier analysis of TRM. *Earth and Planetary Science Letters*, 205(3), pp. 325-336.